Received: 23 October 2018 | Revised: 3 July 2020 | Accepted: 6 July 2020

DOI: 10.1111/jmg.12559

ORIGINAL ARTICLE

Journal of METAMORPHIC GEOLOGY WILEY

Geochronological and petrological constraints from the evolution in the Saxon Granulite Massif, Germany, on the Variscan continental collision orogeny

Jochen Rötzler[1] | **Martin J. Timmerman**[2]

[1]GFZ German Research Centre for Geosciences, Potsdam, Germany

[2]Institute of Geosciences, University of Potsdam, Potsdam-Golm, Germany

Correspondence
Jochen Rötzler, GFZ German Research Centre for Geosciences, Section 3.1, Telegrafenberg, 14473 Potsdam, Germany.
Email: rtzlr@gfz-potsdam.de

Funding information
Deutsche Forschungsgemeinschaft, Grant/Award Number: OB 80/44-1

Abstract

Controversy over the plate tectonic affinity and evolution of the Saxon granulites in a two- or multi-plate setting during inter- or intracontinental collision makes the Saxon Granulite Massif a key area for the understanding of the Palaeozoic Variscan orogeny. The massif is a large dome structure in which tectonic slivers of metapelite and metaophiolite units occur along a shear zone separating a diapir-like body of high-*P* granulite below from low-*P* metasedimentary rocks above. Each of the upper structural units records a different metamorphic evolution until its assembly with the exhuming granulite body. New age and petrologic data suggest that the metaophiolites developed from early Cambrian protoliths during high-*P* amphibolite facies metamorphism in the mid- to late-Devonian and thermal overprinting by the exhuming hot granulite body in the early Carboniferous. A correlation of new Ar–Ar biotite ages with published *P*–*T*–*t* data for the granulites implies that exhumation and cooling of the granulite body occurred at average rates of ~8 mm/year and ~80°C/Ma, with a drop in exhumation rate from ~20 to ~2.5 mm/year and a slight rise in cooling rate between early and late stages of exhumation. A time lag of *c*. 2 Ma between cooling through the closure temperatures for argon diffusion in hornblende and biotite indicates a cooling rate of 90°C/Ma when all units had assembled into the massif. A two-plate model of the Variscan orogeny in which the above evolution is related to a short-lived intra-Gondwana subduction zone conflicts with the oceanic affinity of the metaophiolites and the timescale of *c*. 50 Ma for the metamorphism. Alternative models focusing on the internal Variscan belt assume distinctly different material paths through the lower or upper crust for strikingly similar granulite massifs. An earlier proposed model of bilateral subduction below the internal Variscan belt may solve this problem.

KEYWORDS

geochronology, granulite, high-*P* metamorphism, metaophiolite, Variscan orogeny

1 | INTRODUCTION

Recent attempts to assimilate accumulated geological and geophysical evidence into a plate tectonic model of the late Palaeozoic Variscan orogen in Europe and North-West Africa have renewed the controversy over the involvement of microplates in the Variscan plate convergence. Two models, one being comprehensive in terms of palaeogeography and the other detailed with respect to tectono-metamorphic processes, illustrate the dispute.

The first model, proposed by Kroner and Romer (2013), explains the Variscan belt as due to long-term convergence solely between two major continental plates, Gondwana and Laurussia. Microplates that, according to other models (e.g. Franke, 2000), drifted away from Gondwana to eventually collide and form the internal part of the orogen are interpreted as shelf crust constantly tied to northern Gondwana. Extension-related dissection of this shelf into high-standing blocks of late Neoproterozoic Cadomian basement and subsiding Cambro-Ordovician rift basins created a heterogeneous crustal structure considered to be crucial to later initiation of Variscan intracontinental subduction. The orogeny started in the early Devonian, when oceanic and continental shelf realms of the northward-drifting Gondwana plate plunged below Laurussia. Cadomian magmatic arc crust represented by great thickness in large horst blocks of the peri-Gondwana shelf is believed to have governed a subduction–accretion process in which such unsubductable blocks docked with the upper plate, thereby jamming the subduction zone and causing initiation of a new subduction zone farther inland. The process is supposed to have repeated twice with regard to discrete early Devonian, late Devonian and Viséan high-*P* metamorphic events. After the leading edge of the peri-Gondwana shelf had collided with Laurussia, the Gondwana plate kept moving northward, but the subduction polarity at the plate boundary flipped to the south. This, in conjunction with the initiation of northward-dipping intra-Gondwanan subduction zones, resulted in bipolar subduction below the northern Gondwana margin. The exhumation of high-*P* complexes started at the end of the mid-Devonian and occurred under an overall compressional regime associated with localized extensional tectonics and large-scale strike-slip tectonics that finally shaped the orogen.

The second model, proposed by Schulmann, Lexa, Janoušek, Lardeaux, and Edel (2014) for the internal part of the eastern Variscan belt, assumes multi-plate convergence. Cambro-Ordovician intracontinental rifting of the northern Gondwana margin is accordingly supposed to have proceeded to ocean basin formation and seafloor spreading between microplates that later reassembled into the Variscan orogen. Oceanic crust of the Saxothuringian microplate began subducting beneath the Gondwana margin in the early Devonian, followed by late Devonian to early Carboniferous subduction of continental crust. The eastward subducted oceanic crust developed into a high to ultrahigh-*P* boundary complex separating the Gondwana upper plate from subsequently underthrusted Saxothuringian continental crust. Geophysical profiling data support this interpretation by showing an east-dipping strongly reflective layer correlative with the mafic boundary complex, and a long-wavelength gravity low over the crustal root compatible with subducted Saxothuringian continental crust. Metaophiolites exposed along the postulated suture are the surface expression of the boundary complex, and are the root area of nappe metamorphic rocks transported towards the Saxothuringian foreland of the collision zone. The early orogenic processes conformed to an accretionary system with still well traceable architectural elements, including, from west to east, subduction zone, forearc wedge, magmatic arc, backarc rift, and continental backstop. The forearc wedge thickened by basal accretion of lower-plate continental crust that underwent high to ultrahigh-*P* metamorphism. At the same time, extensional thinning, magmatic heating, and rheological weakening of the crust in the backarc region paved the way for subsequent crustal thickening that occurred in this region when, after the onset of continental collision, slab break-off and isostatic rebound of mantle lithosphere forced forearc wedge crust under the earlier underthrust mafic boundary complex. Heating of the material laterally intruding into the hot lower crust of the former backarc region culminated in high to ultrahigh-*T* metamorphism. The temperature-dependent reduction of the density contrast between orogenic lower and upper crust eventually resulted in gravity overturn and buoyant rise of crustal-scale felsic diapirs now exposed as dome-shaped bodies of high-*P* granulite recording early near-isothermal decompression and subvertical fabric development. The diapirs penetrated the mafic boundary complex and dragged parts of it upwards. Subhorizontal amphibolite facies fabrics and concordant potassic intrusions, dated at *c*. 340 Ma, define a shift from vertical extrusion to horizontal spreading that occurred when the diapirs got stuck below the crustal high-strength lid. The emplacement of the diapirs was concurrent with medium-*P* amphibolite facies metamorphism of vertically foliated country-rock metasediments.

In the plate tectonic model of Schulmann et al. (2014), the Saxon granulites represent Saxothuringian continental crust detached from, and later subducted below, the Gondwana margin. The Caledonian and Variscan basement of the Palaeozoic West European Platform overlying Proterozoic Avalonian and Neoproterozoic peri-Gondwanan crust abuts along the Trans-European Suture Zone against the Precambrian Baltica craton (Figure 1). Feldspar Pb isotope data permitting discrimination between Avalonian and peri-Gondwanan provenances of Variscan basement rocks suggest that the Saxon granulites derive from peri-Gondwanan crust (Jaeckel, Anthes, Molzahn, Oncken, & Reischmann, 1999). Zircon Hf

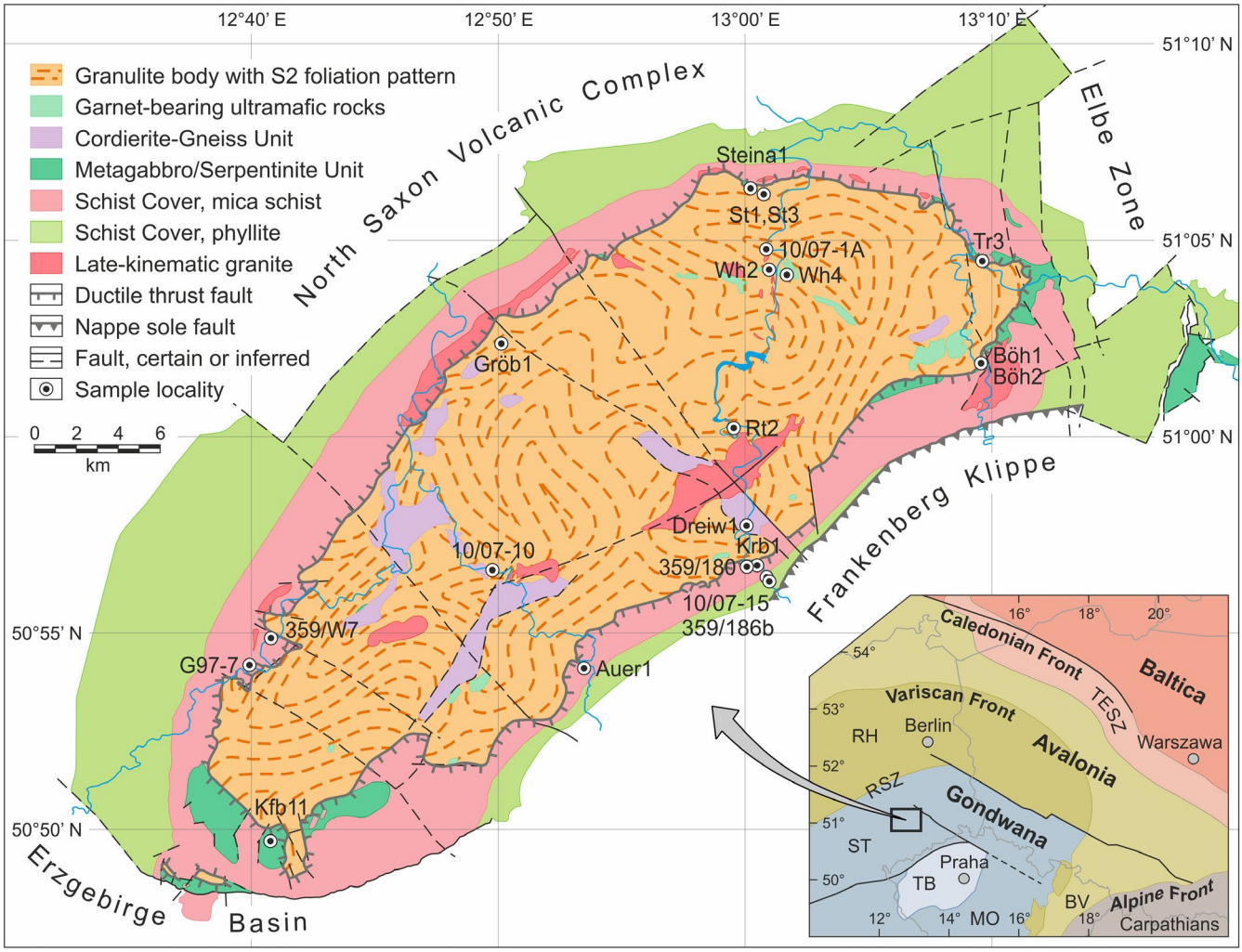

FIGURE 1 Simplified geological map of the Saxon Granulite Massif based on the geological map of Saxony, scale 1:25,000, and a bedrock map devised by Tessin (1989). Teeth on faults refer to the dip direction. The inset map compiled from Kossow (2002), Grad et al. (2008) and Schulmann et al. (2008) shows the tectonic architecture of Variscan central Europe, including the Avalonia-derived Rhenohercynian (RH) and the Gondwana-derived Saxothuringian (ST), Teplá-Barrandian (TB) and Moldanubian (MO) units. The plate tectonic affinity of the Brunovistulian unit (BV) to either Avalonia or peri-Baltica is controversial (Soejono et al., 2017). East Avalonia and the Precambrian Baltica craton abutting each other along the Trans-European Suture Zone (TESZ) merged into the megacontinent Laurussia during the early Palaeozoic Caledonian orogeny. Avalonian and Gondwanan crust meet along the late Palaeozoic Rheic Suture Zone (RSZ)

model ages of the Saxon granulites interpreted as indicating major juvenile crust formation during the Mesoproterozoic seem to contest this. Sagawe, Gärtner, Linnemann, Hofmann, and Gerdes (2016) have therefore assumed an affinity to Baltica caused by subduction erosion of the Baltica margin as the leading edge of the overriding Laurussian plate during Variscan collision with Gondwana. However, this interpretation is ambiguous, as the zircons from the samples used for model age calculation have no Mesoproterozoic crystallization ages. The controversy over the plate tectonic affinity and the evolution of the Saxon granulites in a two- or multi-plate setting during inter- or intracontinental collision makes the Saxon Granulite Massif (SGM) a key area for the understanding of the Variscan orogeny. While much recent research focussing on the granulites as the most prominent rocks of the massif exists, investigating the overlying rocks has proven worthwhile as it unveils important aspects of provenance alongside those of metamorphism and emplacement. Below, we present new geochronological and petrological data on the SGM and review how the plate tectonic models tie in with the enlarged database.

2 | GEOLOGICAL SETTING

The Saxon granulites underlying a 15×44 km^2 oval outcrop area form a NW-vergent, non-cylindrical, regional antiform defined by the main S2 foliation of the rocks (Figure 1). The large, generally NE-SW trending antiform has its crest near the northwestern margin of the outcrop area. The S2

foliation pattern in the core of the granulite body is consistent with steeply plunging folds related to subvertical extrusion (Behr, 1961). Subhorizontal shearing with transposition of S2 into a high-*T* mylonitic S3 foliation is evident in discrete retrograde shear zones associated with the ductile thrust that juxtaposes the granulite body against overlying low-*P* rocks referred to as Schist Cover (Kroner, 1995). This major shear zone contains kilometre-size rafts of two structural units named Cordierite-Gneiss Unit and Metagabbro/Serpentinite Unit after the predominant rocks. The shear zone on top of the exhuming granulite body raised above or lay level with the present-day erosion surface that exposes vestiges of the Cordierite-Gneiss Unit. The Metagabbro/Serpentinite Unit is present as large rafts at the flanks or small pods, not shown in Figure 1, on top of the granulite body. The direct contact of either unit with the granulite body testifies to an excision of structural section. Field evidence does not clearly reveal the vertical, and thus temporal, order in which these units merged with the exhuming hot granulites, but the different thermal overprinting suggests that the Cordierite-Gneiss Unit was first to meet the granulites (Rötzler & Romer, 2010). The granulite body encountered the Cordierite-Gneiss Unit probably before the onset of subhorizontal shearing, as the contact is partially concordant and steep (Behr, 1961). The Schist Cover surrounds the granulite body as an outward-dipping periclinal rim. Mineral stretching lineations change orientation twice in the SGM, showing a gradual swing in trend from NE-SW in the southeast and centre of the granulite body to NW-SE in the shear zone affecting the northwestern flank of the body and the lower part of the Schist Cover. NE-SW trending lineations recur in the hanging wall of the shear zone exposed in the northwestern Schist Cover. The lineation pattern at the southeastern flank of the massif is different, because here the NE-SW trending lineations of the granulite body do not progressively rotate into parallelism with the perpendicularly trending lineations of the Schist Cover (Behr, 1961). Krawczyk et al. (2000) inferred from geophysical profiling data that after the assembly of the structural units, a northwestward travelling and tapering thrust wedge moving up the southeastern flank of the granulite body carried Schist Cover rocks over the granulites. The thrust faults seem to have cut down into the granulite body, where the marginal shear zone within which the lineation had changed direction was truncated. Behr (1961) interpreted the swing in the lineation pattern from NE-SW to NW-SE trending as indicating depth-dependent disharmonic deformation in the same stress field. Kinematic indicators reveal top-to-SW sense of shear during late-stage S2 development, followed by NW-ward underthrusting of the granulite body below the Schist Cover during S3 development (Kroner, 1995). Monzogranite that intruded into the core of the granulite body while the marginal shear zone was still active constitutes undeformed stocks and dykes, whereas coeval intrusions along the shear zone solidified to form foliation-parallel or slightly oblique sheets, which, depending on thickness, have an undeformed core and mylonitic margins (Gottesmann, Tischendorf, & Wand, 1994; Kroner, 1995).

The granulite body is a compositionally and texturally layered complex with a multistage deformation history. Felsic-mafic sequences define an S1 compositional layering that is mostly concordant but not identical with the main S2 foliation because S2 is observed as axial plane foliation of rootless intrafolial folds deforming S1 (Behr, 1961). The S2-parallel felsic-mafic layering accordingly is a transposed sequence, suggesting neither the nature of the protoliths nor their stratigraphy. The mostly fine-grained planar-laminated S2 foliation (Figure S1a) evolved during isothermal decompression from eclogite into granulite facies, as shown by the deep-crustal emplacement of garnet-bearing ultramafic rocks and the preferred orientation of both peak and post-peak minerals parallel to S2. For felsic and mafic granulites, anhydrous peak and decompression mineral assemblages (Figures S2a–e and S3a,b) indicate peak pressures of 2.2–2.3 GPa and significant re-equilibration in the range of 0.9–1.1 GPa, respectively (Rötzler, Hagen, & Hoernes, 2008; Rötzler & Romer, 2001; Rötzler, Romer, Budzinski, & Oberhänsli, 2004). Extensive petrologic investigation has not proved ultrahigh-*P* metamorphism, be it by preserved mineral relics or microtextural evidence. The decompression path was governed by ultrahigh temperatures initially above 1,000°C, as evidenced by single-feldspar, Fe-Mg exchange, Zr-in-rutile and oxygen isotope thermometry as well as by comparison with experimentally determined phase stability relations (Hagen, Hoernes, & Rötzler, 2008; Rötzler & Romer, 2001; Rötzler et al., 2004, 2008; Zack, Moraes, & Kronz, 2004). The coincidence of corona growth with the formation of NE-SW trending mineral lineations on S2 suggests strain heterogeneity at the end of the early exhumation stage. This is obvious in felsic granulite, where undeformed spinel-plagioclase coronas enveloping peak garnet and kyanite in low-strain domains contrast with elongated aggregates of secondary garnet, spinel, and plagioclase defining the lineation in high-strain domains (Figure S2d,e). Exhumation along an increasingly flatter retrograde *P–T* path resulted in partial hydration by fluids invading while the granulite body merged with structurally higher units (Figure S3c,d). Light and dark laminated banding of retrogressed felsic granulite reflects variation in the biotitization of garnet due to small-scale strain partitioning and related channelized fluid infiltration (Figures S1b and S2f).

Each of the upper structural units records a distinct metamorphic evolution until its assembly with the rising granulite body. High-grade metapelites of variable texture and mineralogy exposed in kilometre-size bodies, up to 100 m thick, represent the Cordierite-Gneiss Unit (Figure 1). The rocks consisting of variable modal proportions of quartz,

alkali feldspar, plagioclase, biotite, sillimanite, and either stable garnet or cordierite, are partially massive but more commonly gneissic in texture. Cordierite-bearing migmatitic assemblages predominate over garnet-bearing non-migmatitic ones observed locally at the base of the unit (Figure S1c,d). Reaction textures and consistent bulk-rock X_{Mg} values being at odds with a coeval formation of the garnet and cordierite gneisses suggest that the rocks represent subsequent stages of metamorphism (Figure S4a,b). *P–T* data constrain a clockwise path in which the garnet-forming peak-pressure stage estimated at ~0.6 GPa and 730°C preceded decompression and heating towards the cordierite-forming stage at ~0.5 GPa and 790°C, where the *P–T* path approached that in the rising granulite body (Rötzler & Romer, 2010). Variations in strain rate and fluid activity in the boundary shear zone of the granulite body are likely reasons why garnet gneiss has locally escaped alteration. Chemical and isotopic data support a siliciclastic sedimentary origin but do not indicate a restitic nature of the rocks (Rötzler & Romer, 2010).

The boundary shear zone of the granulite body likewise contains isolated blocks, up to some hundred metres thick, of ultramafic-mafic rocks that are remnants of the once coherent Metagabbro/Serpentinite Unit (MSU). A fault-bounded block located to the southeast of the SGM proper at the Elbe Fault Zone may be an inlier and as such would suggest NW-ward exhumation, or may be due to dextral strike-slip offset along the Elbe Fault Zone (Figure 1). The MSU is a potential correlative of the boundary complex inferred by Schulmann et al. (2014) and is thus important for the debate over the Variscan plate convergence. Kroner, Hahn, Romer, and Linnemann (2007) have argued that the subduction of Saxothuringian crust did not involve oceanic rocks. However, the MSU consisting of metagabbro and metadolerite in the upper part and serpentinized peridotite in the lower part has geochemical signatures typical of an ophiolite (Lünser, 1994). The metagabbros ranging in composition from Ti-rich cumulate to mafic tholeiitic and more felsic calc-alkaline rocks are cross-cut by metadolerite dykes derived from a separate, more evolved magma (Lünser, 1994). In part of the metabasites, relic igneous minerals, such as clinopyroxene, orthopyroxene and calcic plagioclase, are discernible as porphyroclasts or pseudomorphed megacrysts. Igneous amphibole may have existed, but evidence is poor, as fine-grained metamorphic mineral assemblages have replaced most of the igneous mineralogy. The metabasites are mylonite-series products showing a transition from original and pseudomorphed gabbroic textures, through protomylonitic textures with anastomosing foliation around igneous relics, to penetratively foliated textures. NW-SE trending hornblende lineations conform to the above-described lineation pattern in the SGM (Behr, 1961). One objective of our study was to determine the heretofore obscure metamorphic *P–T–t* evolution of the MSU.

The stratigraphy of the Schist Cover documents an inner shelf environment from the early Palaeozoic through to the mid-Devonian, followed by continental slope and near-shore deposition during the late Devonian. With increasing metamorphic grade, the predominant argillaceous rocks transform from slate, unconformably underlying post-orogenic deposits, through phyllite and mica schist, into amphibolite facies sillimanite–biotite schist in contact with the granulite body (Figures S1e,f and S4c,d). The metamorphic zonation developed when the exhuming granulite body conductively heated the Schist Cover. The thermal reworking extends up-section into phyllite, where a NW-SE trending andalusite lineation overprinting an earlier metamorphic fabric manifests heating of already metamorphosed low-grade rocks (Kroner, 1995). *P–T* estimates of 0.3 GPa and 660–680°C obtained at the bottom of the Schist Cover (Rötzler & Romer, 2010) imply post-peak extensional telescoping, as the existing rock column overhead is less than half as thick as required to exert a corresponding, essentially lithostatic pressure. Based on palynomorph stratigraphy, Heuse, Kurze, and Reitz (1994) and Heuse et al. (2010) inferred a Late Neoproterozoic age for deposits higher in the southeastern Schist Cover. If this age were correct, detrital zircon ages indicating younger deposits deeper in the Schist Cover (Rötzler & Romer, 2010) would involve an inverted stratigraphy. Detrital zircon dating undertaken in this study was to verify the age of the palynomorph-bearing deposits and its bearing on the evolution in the SGM.

The SGM borders to the north with the North Saxon Volcanic Complex that covers an area of ~2,000 square kilometres and records the largest late Palaeozoic ignimbrite-forming event in central Europe. The complex is more than 1,300 m thick and rests unconformably on Variscan basement (Walter, 2006). The magmatic activity dated as Early Permian (Asselian-Sakmarian) was simultaneous with volcanism in the Erzgebirge Basin southwest of the SGM (Hoffmann et al., 2013). There, late to post-orogenic volcanism related to terrestrial sedimentation in several superimposed basins collectively referred to as Erzgebirge Basin spanned the time from the late Viséan to the early Permian (Asselian).

3 | PREVIOUS GEOCHRONOLOGY

U-Pb zircon dating using laser ablation-inductively coupled plasma-mass spectrometry (LA-ICP-MS) has recently shed more light on the crustal sources, the protoliths, and the early metamorphic history of the Saxon granulites (Sagawe et al., 2016). Ten per cent of the obtained concordant ages are inherited, clustering in the range from the late Neoproterozoic to the mid-Cambrian, thus coinciding with the Cadomian active margin and the post-Cadomian

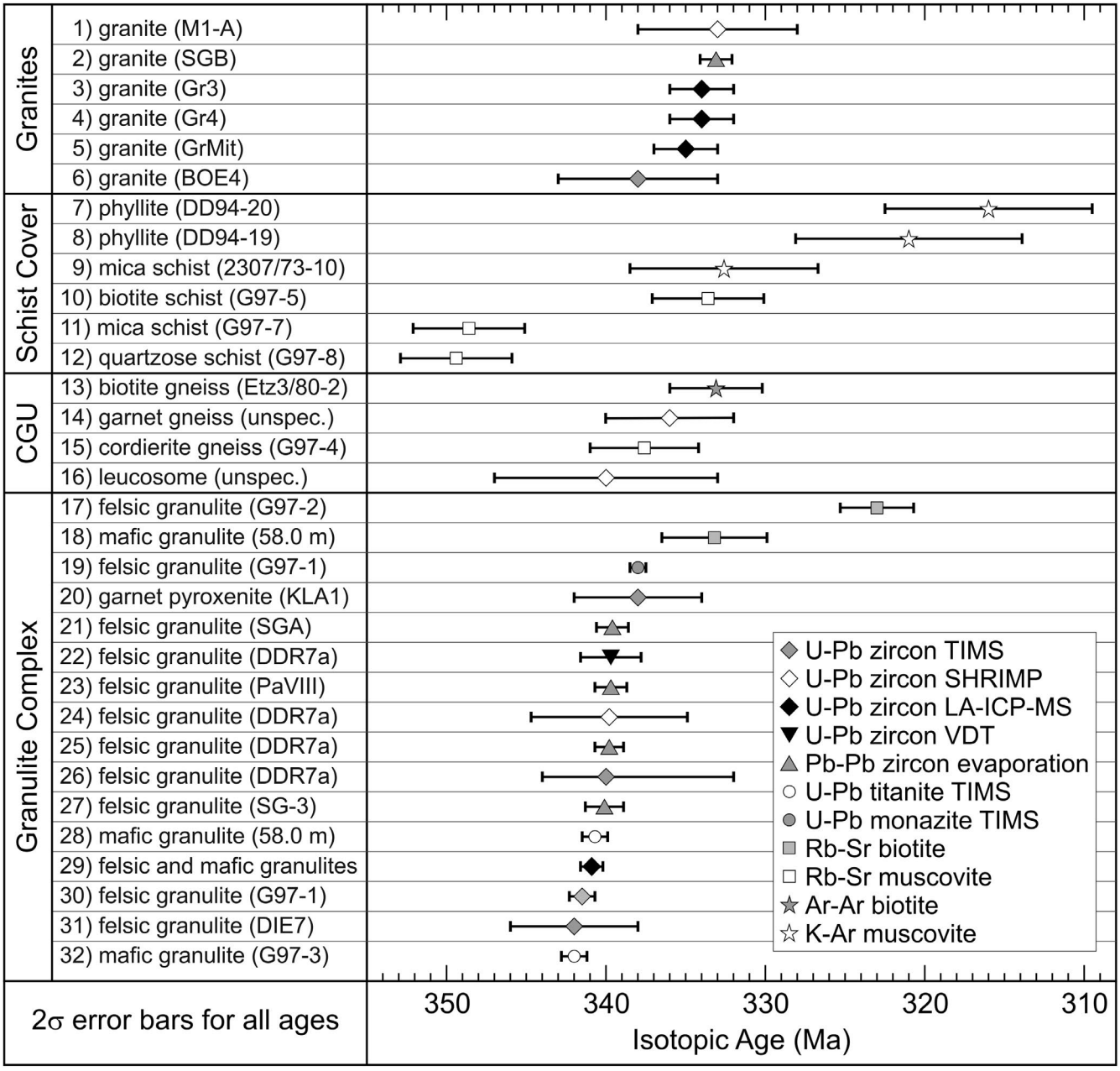

FIGURE 2 Published age data on metamorphism and granite emplacement in the SGM listed from top to bottom in order of increasing age within the structural units. The abbreviations CGU and VDT mean Cordierite-Gneiss Unit and vapour-digestion technique, respectively. Sources are: 1 (Nasdala, Pidgeon, Wolf, & Irmer, 1998); 2, 21–27 (Kröner et al., 1998); 3–5 (Sagawe, Gärtner, Hofmann, & Linnemann, 2013); 6, 20, 31 (von Quadt, 1993); 7, 8 (Marheine, 1997); 9, 13 (Werner & Reich, 1997); 10–12, 15 (Rötzler & Romer, 2010); 14 (Vavra & Reinhardt, 1997); 16 (Vavra, Reinhardt, & Pidgeon, 1999); 17, 19, 30, 32 (Romer & Rötzler, 2001); 18, 28 (Rötzler et al., 2004); 29 is a combined age for eight samples (Sagawe et al., 2016)

continental rift magmatism in northern Gondwana, whereas a few analyses define older Neo- and Palaeoproterozoic ages. Frequency peaks of concordant ages at 494 ± 2 Ma and 450 ± 2 Ma correspond to two phases of protolith formation during Cambro-Ordovician continental rift magmatism. This interpretation supports results from SHRIMP and ID-TIMS U–Pb studies of zircon and titanite suggesting protolith formation of felsic granulite at *c*. 485–473 Ma (Kröner, Jaeckel, Reischmann, & Kroner, 1998), and of metatholeiitic mafic granulite at 499 ± 2 Ma (Rötzler et al., 2004). The Cambro-Ordovician protolith ages of felsic and mafic granulites agree with each other within uncertainty, thus throwing doubt on a Late Devonian protolith age of metatholeiitic mafic granulite inferred by Sagawe et al. (2016) from a lack of older concordant zircon, except a single Early Devonian age, in their only sample of

this rock type. The Cambro-Ordovician protolith ages of the Saxon granulites overlap with U–Pb zircon ages in the range 500–470 Ma obtained throughout the Variscan belt for a late stage of rift magmatism in the northern Gondwana margin (e.g. Díez Fernández, Pereira, & Foster, 2015; Höhn et al., 2018; Kryza & Fanning, 2007; Kusbach et al., 2015; Tichomirowa, Sergeev, Berger, & Leonhardt, 2012). Another age population of the Saxon granulites dated by Sagawe et al. (2016) to *c*. 406 Ma is of uncertain magmatic or metamorphic origin. Zircons with age frequency peaks *c*. 375, 357 and 341 Ma are most common, showing internal structures typical of metamorphic growth. The major age peak *c*. 341 Ma confirms previous interpretations relating U–Pb zircon and titanite ages in the range 342–340 Ma to the peak of metamorphism. Rb-Sr biotite ages of 333 ± 3 Ma obtained at the margin and of 323 ± 2 Ma at the centre of the granulite body define the time of isotopic closure of this system (references in the caption to Figure 2).

SHRIMP U–Pb zircon dating of the Cordierite-Gneiss Unit has yielded ages of 600–550 Ma for detrital grains and *c*. 490 Ma for prismatic overgrowths (Vavra & Reinhardt, 1997). Consequently, the protoliths are of Cambrian or Early Ordovician age, depending on whether the zircon rims are metamorphic (Reinhardt & Vavra, 1997) or were formed in a magma body prior to volcanic input into the protoliths (Rötzler & Romer, 2010). Isometric zircon crystals in garnet gneiss with a minimum age of 336 ± 4 Ma and zircon in leucosome of cordierite gneiss grown 340 ± 7 Ma date high-grade conditions near or at the thermal peak of metamorphism. An Rb-Sr age of 338 ± 3 Ma on retrograde muscovite and an Ar–Ar biotite age of 333 ± 3 Ma define the time of isotopic closure of the muscovite Rb–Sr and biotite K–Ar systems in the Cordierite-Gneiss Unit (references in the caption to Figure 2).

SHRIMP U–Pb dating revealed that sillimanite–biotite schist of the Schist Cover has Neoproterozoic zircon detritus overgrown by *c*. 487 Ma old zircon rims (Vavra & Reinhardt, 1997). This suggests an Early Palaeozoic protolith age at the base of the Schist Cover, with the same interpretations as those discussed above for the Cordierite-Gneiss Unit. Rb–Sr and K–Ar muscovite ages of *c*. 349 Ma, *c*. 334–333 Ma and *c*. 321–316 Ma obtained on metasediments of the Schist Cover constrain the time of isotopic closure after (a) metamorphism unrelated to the emplacement of the granulite body, (b) heating by the underthrusted granulite body and (c) reheating during post-orogenic magmatism (references in the caption to Figure 2).

The late-kinematic granite intrusions in the granulite body and its boundary shear zone have yielded zircon ages in the range 335–333 Ma based on pooled data from spot and single-grain measurements, and an upper intercept age of *c*. 338 Ma for discordant multigrain zircon fractions (references in the caption to Figure 2).

4 | ANALYTICAL METHODS

We summarize here the analytical methods described in detail in Appendix S1. Following thin-section examination, 18 of 21 selected rock samples were processed by conventional techniques to obtain zircon, amphibole, biotite and white mica separates that were manually purified under a stereomicroscope. Extensive electron probe microanalyses provided a basis for phase equilibria modelling and Ti-in-zircon thermometry, and allowed checking the Ar–Ar dated minerals for chemical inhomogeneities that may affect the argon gas release spectra. Two samples, one of metagabbro and one of metapelite, yielded enough zircons for LA-ICP-MS analysis. Scanning electron microscopy helped in selecting zircons for U–Pb dating and rare earth element (REE) analysis of polished mounted grains. Internal zircon structures were studied using back-scattered electron (BSE), secondary electron, and cathodoluminescence imaging. Energy-dispersive X-ray spectroscopy facilitated identifying mineral inclusions in zircon. The irradiation for $^{40}Ar/^{39}Ar$ mineral dating was done in four batches and incremental step-heating analyses using a CO_2 laser were carried out on aliquots of 3 (micas) to 8–30 grains (amphibole, depending on grain size). Appendix S1 specifies the instrumentation, experimental conditions, reference materials, data reduction methods and plateau criteria.

5 | PETROGRAPHY

The studied 21 rock samples taken from all structural units of the SGM (Figure 1, Appendix S2) include 16 Ar–Ar dated samples, one U–Pb dated sample (359/186b), one sample dated by both methods (Steina1) and three samples from the MSU (Böh1, 359/180, Kfb11) used solely for petrologic investigation.

5.1 | Granulite Complex

The six samples taken from the Granulite Complex served for $^{40}Ar/^{39}Ar$ biotite dating. Mafic two-pyroxene granulite (sample Rt2) gathered from centimetre- to decimetre-scale layered felsic-mafic granulite shows a granoblastic lobate texture of fine-grained clinopyroxene, orthopyroxene, antiperthitic plagioclase, and quartz. Millimetre-scale platy quartz grains coalesced into widely spaced quartz ribbons and the shape-preferred orientation of quartz and pyroxene in the matrix define a distinct foliation. Overprinting of this texture, first by foliation-parallel growth of biotite, amphibole and ilmenite, then by discordant actinolite–chlorite veinlets records a two-stage retrograde evolution. Retrograde biotite aligned in the foliation was dated. Prismatine-bearing felsic granulite (sample 10/07-1A) collected at the type locality of prismatine

forms biotite-poor anatectic melt pockets and veinlets in a metre-scale lens of indistinctly foliated, biotitized, felsic granulite. Texture and modal mineralogy of either part of the lens that lies within meta-igneous felsic granulite vary strongly. For detailed accounts of the petrography and metamorphic evolution of the prismatine-bearing granulite, see Grew (1986), Hagen et al. (2008) and Rötzler et al. (2008). In the studied sample, double-layer coronas on relic millimetre-size garnet grains consisting of an inner layer of biotite associated with montmorrilonite–quartz symplectite that likely is an alteration product of cordierite, and an outer layer of radiating sprays of chlorite reflect a two-stage retrograde evolution. We sampled biotite from the corona around a single large garnet grain for Ar–Ar dating. A retrogressed feldspar-rich granulite (sample Wh4) has similarity in mineralogy to the prismatine-bearing granulite but differs by the presence of a foliation. The three texturally distinct mineral assemblages in this rock are (a) a medium- to coarse-grained assemblage of unaligned perthitic alkali feldspar, corundum, rutile, accessory tourmaline and pyrite, (b) a fine-grained assemblage of biotite, spinel, sillimanite and plagioclase that defines an anastomosing S2 foliation around relic domains of the proto-mylonitized early assemblage and (c) a late assemblage of unaligned muscovite and chlorite. Biotite of the foliated assemblage was dated. Two other samples represent ordinary retrogressed felsic granulites. In a faintly foliated rock overprinted under static condition (sample Wh2), coarse coronitic biotite used for Ar–Ar dating encircles masses of fine biotite pseudomorphic after garnet. The second sample of this rock type (sample St3) has a planar-laminated foliation defined by quartz and biotite ribbons that alternate with quartz-feldspar masses mottled with biotite. Biotite aligned in the foliation was dated. A biotite granite dyke (sample St1) cutting across retrogressed mafic granulite has an inequigranular texture of quartz, plagioclase and K-feldspar. Dispersed biotite flakes used for Ar–Ar dating have locally passed into chlorite.

5.2 | Cordierite-Gneiss Unit

The two Ar–Ar dated samples from the Cordierite-Gneiss Unit include metapelitic biotite–garnet–sillimanite gneiss (sample 10/07-10) in which reaction textures show a transition from garnet-producing to cordierite-producing metamorphism. The fine- to medium-grained rock contains semi-euhedral broken garnet grains enveloped in narrow cordierite coronas. More massive cordierite interstitial between garnet grains resorbs coarse ragged biotite flakes with inclusions of rutile, zircon and monazite. Sillimanite, cordierite, spinel and ilmenite occur in diablastic textures replacing garnet, biotite and rutile. Biotite–sillimanite trails defining a widely spaced foliation anastomose around garnet and its reaction products. Thus, the assemblage cordierite–sillimanite–spinel–ilmenite has overprinted the assemblage garnet–biotite–sillimanite–rutile while K-feldspar, plagioclase and quartz have invariably been present. We separated large biotites from the early mineral assemblage for Ar–Ar dating. Amphibole fels (sample Dreiw1) collected from mafic pods within cordierite gneiss consists of a fine-grained matrix of randomly oriented amphibole, ilmenite and accessory apatite, interspersed with medium-grained amphibole porphyroblasts. The matrix contains relics of igneous minerals, such as clinopyroxene, spinel and chromite. Bastite, chlorite and siderite–quartz aggregates with locally associated sphalerite developed during retrogression. Quartz occurs only in this late metamorphic assemblage. Porphyroblastic amphibole was Ar–Ar dated.

5.3 | Metagabbro/Serpentinite Unit

Among the eight samples from the MSU studied petrologically, four were Ar–Ar dated, and one was Ar–Ar and U-Pb dated. The samples reflect the gabbro-amphibolite transition in the MSU that ranges from preserved gabbro textures to pervasively metamorphosed amphibolite, with variations in texture and mineralogy at the outcrop or smaller scales. The least affected rock type is unfoliated metagabbro (sample Böh2) showing granoblastic domains of exsolved clinopyroxene overprinted along grain boundaries by amphibole and ilmenite (Figure 3a). However, a texture in which amphibole–plagioclase intergrowths intervene between igneous plagioclase relics and amphibole masses enclosing igneous clinopyroxene is more common. A conspicuous feature is bastitization of clinopyroxene along fissures or

FIGURE 3 Microphotographs: (a) Interstitial metamorphic amphibole spreads along grain boundaries of a local relic gabbro texture formed by exsolved clinopyroxene; crossed polars (Böh2). (b) Fine metamorphic amphibole and plagioclase–quartz masses are pseudomorphic after a medium-grained gabbro texture; crossed polars (Steina1). (c) Masses of fine-grained amphibole defining the foliation in mylonitic amphibolite contain amphibole porphyroclasts; crossed polars (Böh1). (d) Coronitic garnet encircles relic igneous orthopyroxene; crossed polars (359/180). (e) Skeletal garnet grows on relic igneous plagioclase; half-crossed polars (Kfb11). (f) Chlorite cuts a crushed garnet grain sandwiched between amphibole-rich and plagioclase-rich layers in garnet amphibolite; plane-polarized light (Krb1). (g) Tightly folded sillimanite–biotite trails occur between less strained quartz domains in high-grade sillimanite–biotite schist from the base of the Schist Cover; plane-polarized light (Tr3). (h) S-C mylonitic micaceous quartzite from a higher structural level of the Schist Cover contains lenticular muscovite fish (sigma clasts) with tails defining a shear band cleavage (C-planes) oblique to the mylonitic foliation (S-planes); crossed polars (10/07-15). Mineral abbreviations are from Whitney and Evans (2010)

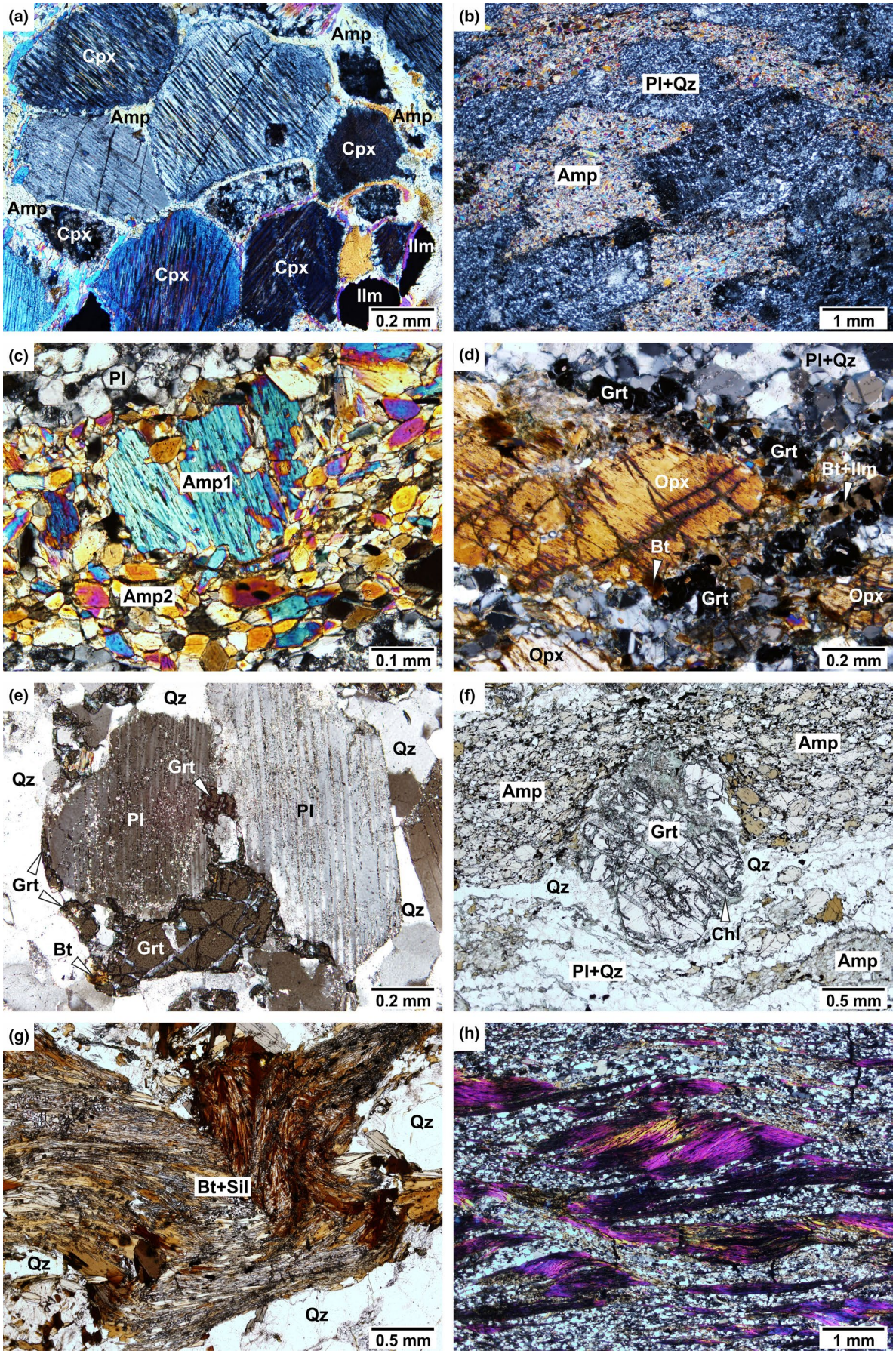
(a)
Cpx
Amp
Amp
Amp
Cpx
Amp
Cpx
Cpx
Cpx
Ilm
Ilm
0.2 mm
(b)
Pl+Qz
Amp
1 mm
(c)
Pl
Amp1
Amp2
0.1 mm
(d)
Pl+Qz
Grt
Grt
Bt+Ilm
Opx
Bt
Grt
Opx
Opx
0.2 mm
(e)
Qz
Qz
Grt
Qz
Pl
Pl
Grt
Qz
Bt
Grt
0.2 mm
(f)
Amp
Amp
Grt
Qz
Qz
Chl
Pl+Qz
Amp
0.5 mm
(g)
Qz
Bt+Sil
Qz
Qz
0.5 mm
(h)
1 mm

by penetrative clouding. Ilmenite commonly sheathed by titanite, and pyrite are accessories. Amphibole Ar–Ar dating of sample Böh2 included two grain-size fractions: a coarser fraction of dark-coloured equant grains (Amp1) and a finer one of light-coloured prisms (Amp2). Another example of this rock type (sample Steina1) exhibits fine amphibole and plagioclase-quartz masses pseudomorphing a gabbro texture with rare relics of igneous minerals (Figure 3b). This texture passes locally into mylonite shear zones with amphibole–plagioclase–ilmenite foliation and minor aligned biotite. Amphibole oriented parallel to the shear-zone foliation was Ar–Ar dated. Pervasively mylonitized amphibolite with anastomosing (sample Böh1) or layered (sample Gröb1) foliation represents the second rock type. The mylonitic matrix surrounds aligned porphyroclasts of igneous minerals. Some amphibole aggregates decrease in grain size from core to rim (Figure 3c) or display a core of fibrous bastite clouded with opaque dust as a reaction product of pyroxene. Cross-cutting amphibole laths, biotite sprays overgrown on amphibole and unaligned chlorite suggest post-mylonitic overprinting. For Ar–Ar dating, we extracted largely inclusion-free matrix amphiboles from sample Gröb1. Fine-grained garnet-bearing amphibolites indicate higher degrees of metamorphic recrystallization. In sample 359/180, some layers preserve quartz ribbons and orthopyroxene porphyroclasts overgrown by coronitic garnet (Figure 3d), whereas other layers, formed by the assemblage garnet–amphibole–biotite–ilmenite–plagioclase–quartz, may have attained equilibrium. The garnet underwent local chloritization. Sample Kfb11 has garnet only in a slightly discordant quartz-plagioclase vein, ~2 mm wide, and in host rock adjacent to the vein. The garnet forms skeletal overgrowths on plagioclase in the vein (Figure 3e) and poikiloblastic intergrowths with amphibole and ilmenite in the host rock. Rutile included in ilmenite, and chlorite replacing biotite occurs in the host rock and the vein. Sample Auer1 represents the third rock type at which the gabbro-amphibolite transition terminates. It is a fine-grained amphibolite with granoblastic amphibole–plagioclase texture but only traces of garnet. Quartz fills grain interstices of amphibole, whereas ilmenite and biotite occur intergrown with amphibole. The assemblage chlorite–calcite–titanite–quartz developed during retrograde overprinting. Sample Krb1 is more abundant in garnet, showing a granoblastic garnet–amphibole–biotite–ilmenite–plagioclase–quartz texture, with some layering defined by variation in the proportions of amphibole and plagioclase. The euhedral to semi-euhedral garnet is commonly broken and partially chloritized (Figure 3f) or is totally replaced by radial sprays and masses of chlorite. Apatite and pyrite are accessories. The single generations of amphibole present in the samples Auer1 and Krb1 were Ar–Ar dated.

5.4 | Schist Cover

Sampling of the Schist Cover aimed at Ar–Ar mineral dating and detrital U-Pb zircon dating of metamorphic rocks. A body of fine- to medium-grained, indistinctly foliated amphibolite (sample 359/W7) lying concordantly within high-grade schist is formed mainly by amphibole, plagioclase, ilmenite and titanite. Mineral textures show that the peak assemblage amphibole–plagioclase–biotite–ilmenite preceded the retrograde assemblage chlorite–sericite–prehnite–albite–titanite–hematite. Epidote and quartz occur as patches and in fractures of the rock. Amphibole was Ar–Ar dated. In fine- to medium-grained sillimanite–biotite schist (sample Tr3), strain partitioning is evident from strained sillimanite−biotite trails (Figure 3g) alternating with biotite–sillimanite–ilmenite clusters, K-feldspar, quartz and minor plagioclase in low-strain domains. Corroded biotite and quartz enclosed in K-feldspar hint at a K-feldspar producing reaction. Muscovite replacing K-feldspar, sillimanite and biotite developed during retrogression. When separating large aligned biotite flakes for Ar–Ar dating, we tried to avoid as much as possible sillimanite intergrowths. The muscovite yield from sample Tr3 was too low for dating. Three other samples collected increasingly farther away from the granulite contact carry prograde muscovite. Fine-grained quartz–mica schist (sample G97-7) composed of alternating quartz–plagioclase layers and thin sillimanite–biotite–muscovite layers has accessory tourmaline, apatite, zircon and retrograde chlorite. Biotite and muscovite aligned in the foliation were Ar–Ar dated. In S-C mylonitic micaceous quartzite (sample 10/07-15), a quartz fabric with disseminated biotite, muscovite and chlorite defines S-planes containing millimetre-size muscovite fish as sigma clasts from which thin muscovite trails emanate into C-planes as a shear band cleavage (Figure 3h). Muscovite fish were Ar–Ar dated. Graphite-bearing quartz–mica schist (sample 359/186b) intercalated with metabasite has yielded palynomorph microfossils of uncertain Neoproterozoic age (Heuse et al., 1994, 2010). The upper greenschist to amphibolite facies rock with alternating phyllosilicate and quartz-rich layers has a wavy to crenulated foliation parallel to compositional layering. The phyllosilicate layers comprise mainly muscovite and variable proportions of biotite, chlorite and graphite, partially accompanied by euhedral garnet or chiastolitic andalusite. Round graphitic structures and fragments may correspond to microfossils. Because of the fine grain size and strong intergrowth of biotite and muscovite, the sample has proved unsuitable for Ar–Ar mica dating. It has instead yielded detrital U–Pb zircon ages.

6 | MINERAL CHEMISTRY

We have used the spreadsheet of Locock (2014) based on the International Mineralogical Association's amphibole nomenclature (Hawthorne et al., 2012) to classify amphibole compositions in one metabasite from each the CGU and the Schist Cover, and in five metabasites that record the gabbro-amphibolite transition in the MSU. All but one of the analyses corresponds to calcic amphibole, represented mainly by magnesio-hornblende and, to a lesser extent, magnesio-ferri-hornblende and actinolite, but only rarely by pargasite and ferri-tschermakite. The only exception is cummingtonite analysed from sample Böh2 (Appendix S3). In most samples, the amphibole composition varies strongly, showing increasing contents of Al, Ti, Na and K with decreasing Si contents at constant or slightly decreasing X_{Mg} (Mg/ [Mg+Fe^{2+}]) (Figure 4). X_{Mg} of the amphiboles ranges from peak values of 0.86–0.88 in the most mafic rocks (Steina1, Dreiw1) to minimum values of 0.56–0.60 in more felsic rocks (359/W7, Auer1, Krb1). Rim-to-rim line scans across individual amphibole porphyroblasts from sample Dreiw1 show asymmetric zoning or opposite zoning trends to rims lower or higher in Si content. Lenticular amphibole aggregates from sample Gröb1 have rims lower in Si content. However, the sample Krb1 consisting of a granoblastic peak-metamorphic mineral assemblage clearly indicates the amphibole compositional evolution in the MSU in that its tightly clustered amphibole compositions represent the upper end of the established composition range at the hornblende–pargasite boundary (Figure 4). The data obtained from the less well-equilibrated sample Auer1 of this rock type, albeit showing wide variation, have a focus similar to that of sample Krb1. The amphibole compositional variation preserved in metabasites from the CGU and the MSU is thus a result mainly of prograde metamorphic recrystallization but also of some retrograde re-equilibration. Metabasite from the high-grade zone of the Schist Cover (sample 359/W7) carries magnesio-hornblende overprinted by minor retrograde actinolite.

Biotite analysed from rocks within each metamorphic unit show that in most samples the biotite compositional variation is low. The whole dataset (Appendix S4) outlines a decrease in Al content while X_{Mg} increases from 0.29 for biotite in quartz–mica schist from the Schist Cover to values ~0.77 for biotite in prismatine-bearing granulite from the granulite

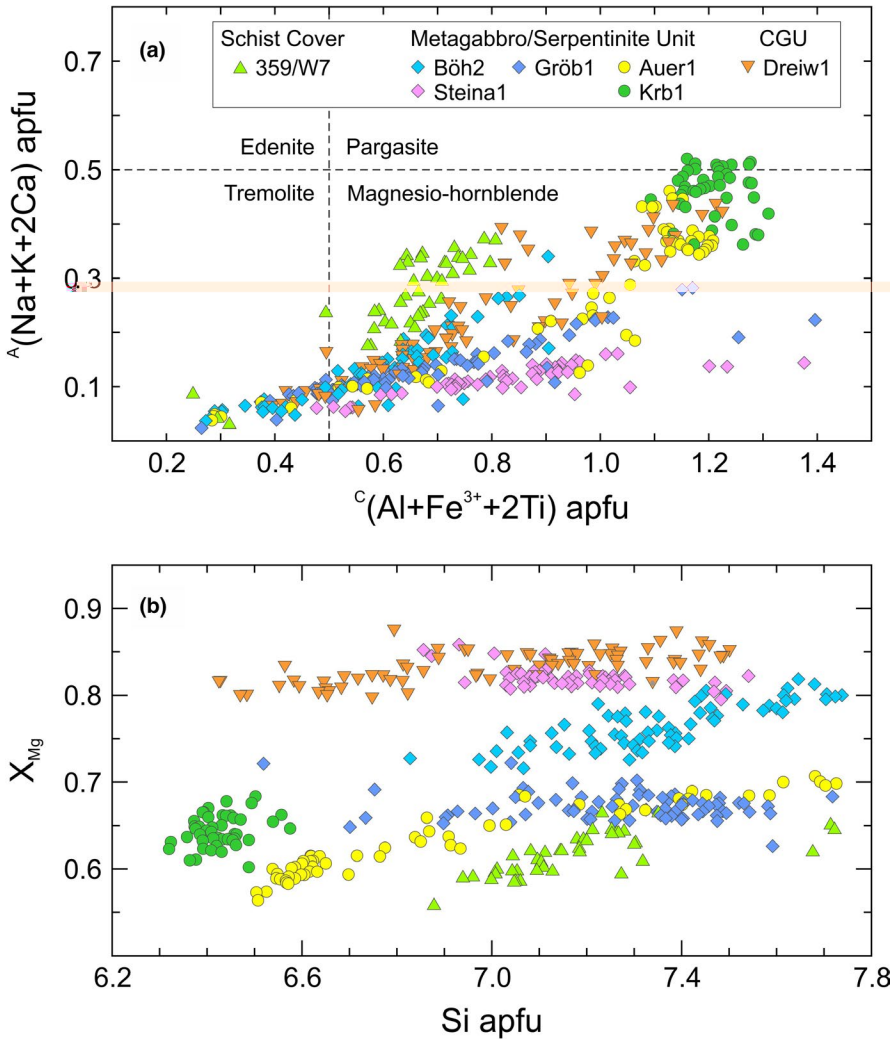

FIGURE 4 Variation in amphibole composition observed in metabasites of the metamorphic units above the granulite body: (a) Contents of Al+Fe^{3+}+2 Ti in C-sites versus those of Na+K+2 Ca in A-sites in atoms per formula unit (apfu), (b) Si contents in apfu versus X_{Mg}. Cordierite-Gneiss Unit is abbreviated as CGU. For corresponding Ar–Ar age data, see Figures 14 and 15

body (Figure 5). Significant intra-sample scatter in biotite composition is evident only for the studied retrogressed felsic and feldspar-rich granulites, where small changes in X_{Mg} of biotite coincide with widely variable Al contents. This variation in composition reflects different textures and mineral assemblages. In retrogressed felsic granulites (St3, Wh2), biotite is intergrown with sillimanite and/or ilmenite and is dispersed in the matrix or coalesced into bands, or it surrounds and replaces garnet. The matrix biotite representing an early generation have higher X_{Mg} and lower Al content than biotite from local equilibrium domains at garnet rims and in places of former garnet (see also Rötzler et al., 2004). Biotite from retrogressed feldspar-rich granulite (Wh4) encompasses two groups with different Al and Ti contents but nearly identical X_{Mg}. We interpret the low-Al, high-Ti biotite observed solely as inclusions in alkali feldspar as a relic early generation undigested by the anatectic melt that crystallized to form the early mineral assemblage of unaligned alkali feldspar, corundum and rutile. High-Al, low-Ti biotite included in corundum of the early assemblage compares closely in composition with biotite from the foliation-defining biotite–spinel–sillimanite–plagioclase assemblage, suggesting that crystallization from melt and foliation development took place in close succession at similar *P–T* conditions. An interpretation that the biotite inclusions in corundum could be secondary in origin and have equilibrated with the foliation-defining assemblage seems unsound as, apart from biotite, corundum has inclusions of spinel that differ from matrix spinel by higher X_{Mg} and lower Zn content.

White micas analysed from quartzose metasediments of the Schist Cover have compositions close to end-member muscovite (Appendix S5), with average Si contents of 3.06–3.10 cations per 11 oxygens. The Ti contents are low, averaging consistently 0.02 cations per 11 oxygens in either sample. X_{Na} [Na/(Na+K)] values ~0.10 and X_{Mg} values ~0.30 measured on sample 10/07-15 are below the respective mean values of 0.12 and 0.40 for sample G97-7. The data plot close to the Tschermak substitution line along which divalent cations substitute for aluminium in the octahedral sites, thereby causing a charge deficiency that allows silicon to enter more tetrahedral sites. Small deviations from this line are likely due to neglected substitutions, mainly of titanium, and the assumption that all iron is ferrous (Figure 6).

Garnet analysis undertaken to investigate the metamorphism of the MSU has involved four samples of garnet-bearing amphibolite. The rocks with the peak mineral assemblage garnet–clinoamphibole–biotite–ilmenite–plagioclase–quartz are variably abundant in garnet and vary in the degree of equilibration during peak metamorphism. The garnets are grossular–pyrope–almandine solid solution forming unzoned to clearly zoned grains. The garnet compositions from the individual samples, plotting along the compositional trend displayed by zoned crystals, suggest differences in the effective bulk chemistry of the rocks, but may also reflect differences in *P–T* conditions and time of garnet growth (Figure 7). Garnet made up of <60 mol.% almandine, >15 mol.% pyrope, and ~25 mol.% grossular constitutes the core of zoned crystals and the total garnet population in sample Kfb11. Zoned crystals show an increase in pyrope content to >20 mol.% and a reversed trend in grossular content at little variable almandine content from the core to an inner zone similar in composition to the total garnet population in sample Krb1. Outer rims of zoned crystals and much of the garnet population in sample 359/180 have almandine contents ~65 mol.% at pyrope and grossular contents <20 mol.% (Appendix S6).

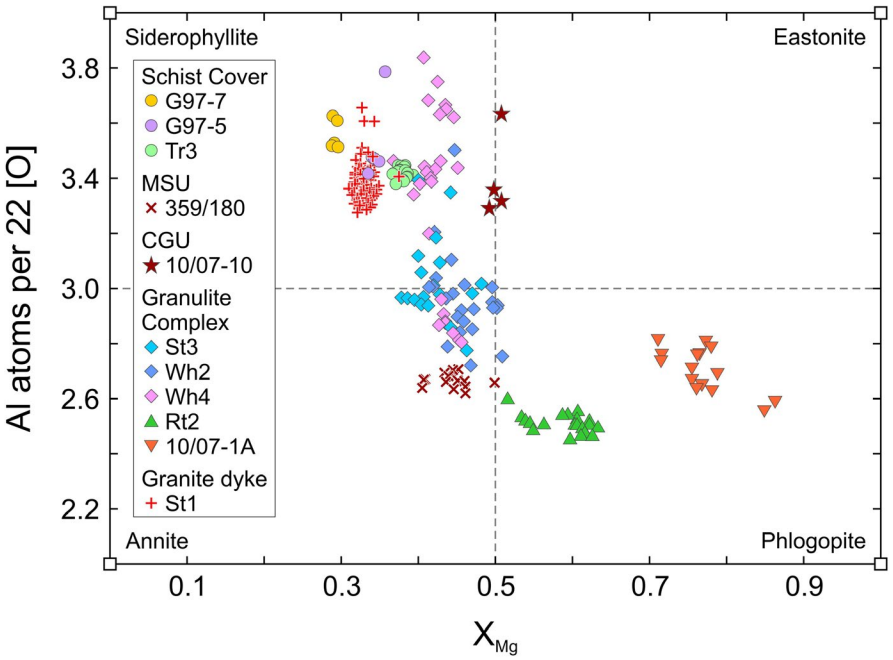

FIGURE 5 Variation in biotite composition observed in metasedimentary and meta-igneous rocks of the SGM. For corresponding Ar–Ar age data, see Figures 15 and 16

Feldspars analysed from the metabasite samples of the MSU comprise relic magmatic plagioclase intermediate between labradorite and bytownite (An50-90), and metamorphic plagioclase varying mainly within the range of andesine (An30-50). In the rims of relic magmatic plagioclases the anorthite content may decrease to near 50 mol.%. The variation in composition between and within the metamorphic plagioclase populations depends on bulk-rock chemical differences but mainly reflects a lack of equilibrium. The mineral chemical evolution is evident from zoned crystals of metamorphic plagioclase showing generally an increase in anorthite content from core to rim, with maximum contents at or slightly above 50 mol.%. In sample Krb1, where granoblastic texture and a dense cluster of amphibole compositions suggest equilibrium, the anorthite content rises from 38 to 42 mol.% in the core to 47–56 mol.% in the rim of plagioclase (Appendix S7).

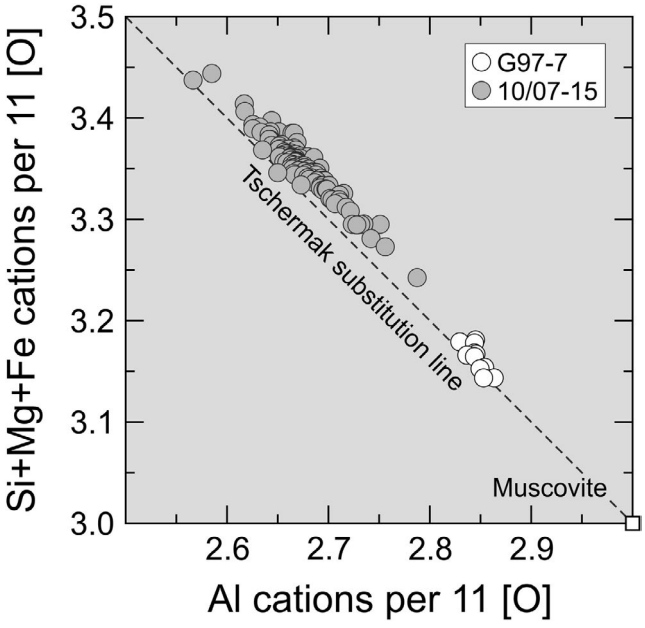

FIGURE 6 Variation in white mica composition observed in two metasediment samples from the Schist Cover of the SGM dated by Ar–Ar geochronology (see Figures 15 and 16)

7 | PSEUDO-SECTION MODELLING

The sample Krb1 has proved to be the most suited among the samples studied for determining the peak metamorphic *P–T* conditions in the MSU, considering its granoblastic texture, lack of igneous mineral relics, and little variable amphibole and garnet compositions. Phase equilibria modelling using Theriak-Domino software (de Capitani & Petrakakis, 2010) in combination with the tcdb55c2d database (Holland & Powell, 1998) has allowed comparing the predicted with the observed mineral assemblages and compositions. We have based the calculations on the bulk-rock chemistry of sample 86003 from Wirth (1989). This sample originates from the same locality and rock type as sample Krb1 and has been

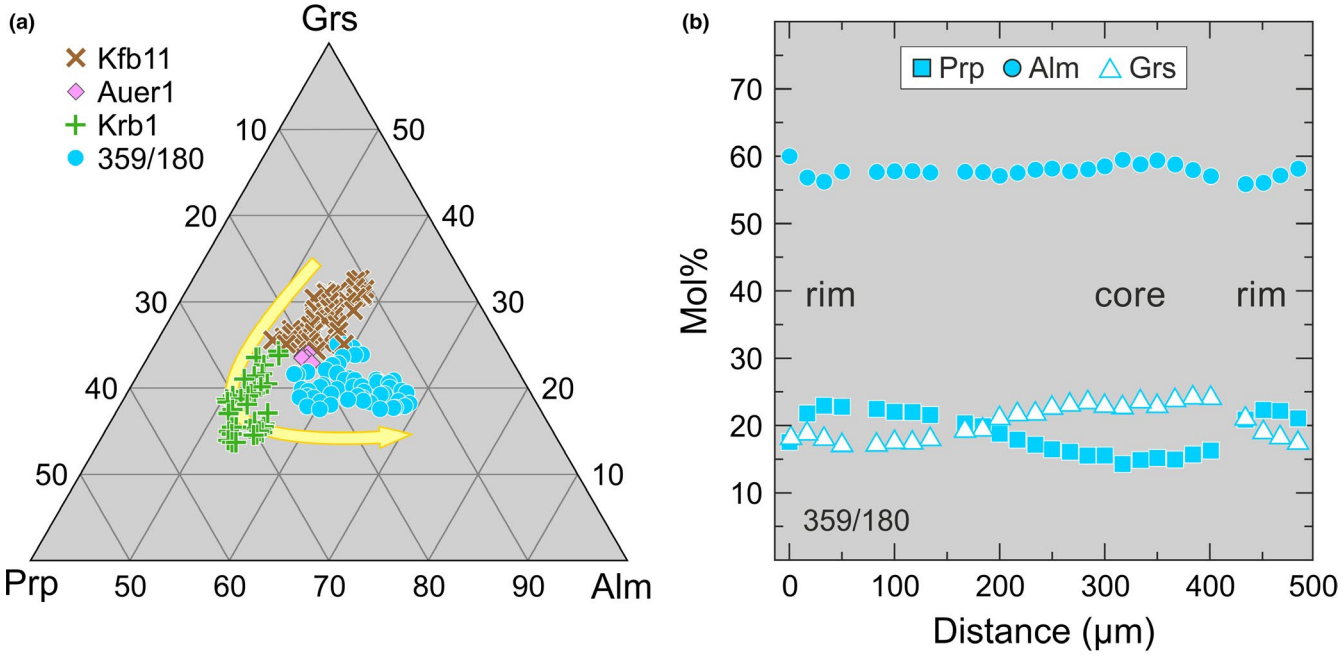

FIGURE 7 (a) The garnet composition in amphibolites from the Metagabbro/Serpentinite Unit of the SGM records an initial trend of decreasing grossular and increasing pyrope contents and a subsequent trend of decreasing pyrope and increasing almandine contents (arrow). (b) The zoning pattern of single crystals conforms to these trends, albeit the compositional range for garnet from the entire rock association is wider

described as consisting by volume of 58% mafic silicates, 34% plagioclase and 8% ilmenite, which is closely similar to the volume proportions of sample Krb1 determined by conventional point counting as 55% mafic silicates, 32% plagioclase, 7% quartz and 6% ilmenite. The mafic silicates comprise 47% amphibole, 2% biotite, 1% garnet and 5% retrograde chlorite. A simplification of the bulk-rock chemistry of sample 86003 into the system Na_2O–CaO–K_2O–FeO–MgO–Al_2O_3–SiO_2–H_2O (NCKFMASH) has neglected minor components, above all TiO_2. De Capitani and Petrakakis (2010) used the system NCKFMASH for phase equilibria modelling of the peak assemblage in ilmenite-bearing metapelite, thus neglecting TiO_2, and found that the modelling results were in excellent agreement with thermobarometric *P*–*T* estimates. They stressed that, in the current absence of reliable solution models incorporating the complete compositional range of the minerals, there is uncertainty about the effect that including minor components has on phase equilibria modelling results, especially with respect to the correct prediction of mineral composition isopleths. A simplified chemical system is thus favourable for the prediction of mineral composition isopleths needed to constrain the equilibrium *P*–*T* conditions in the wide stability range of the mineral assemblage in sample Krb1. Our calculations assumed water in excess.

The modelling results suggest that the assemblage garnet–clinoamphibole–biotite–plagioclase–quartz present in sample Krb1 is stable within a wide *P*–*T* range abutting against the stability ranges of chlorite at lower temperature, coexisting clinoamphibole phases at lower pressure, zoisite at higher pressure and a melt phase at higher temperature (Figure 8). When relating the analysed to the modelled compositions of garnet and plagioclase, it becomes evident that the *P*–*T* conditions attained during peak metamorphism were slightly above 1.0 GPa and 700°C. Moreover, the discovered mineral compositional trends from grossular-rich, through pyrope-rich, to almandine-rich garnet, and from lower to higher anorthite plagioclase record a clockwise near-peak *P*–*T* path. However, whereas the predicted and analysed contents of anorthite in plagioclase and of grossular in garnet agree favourably, those of pyrope and almandine in garnet do not, with the prediction

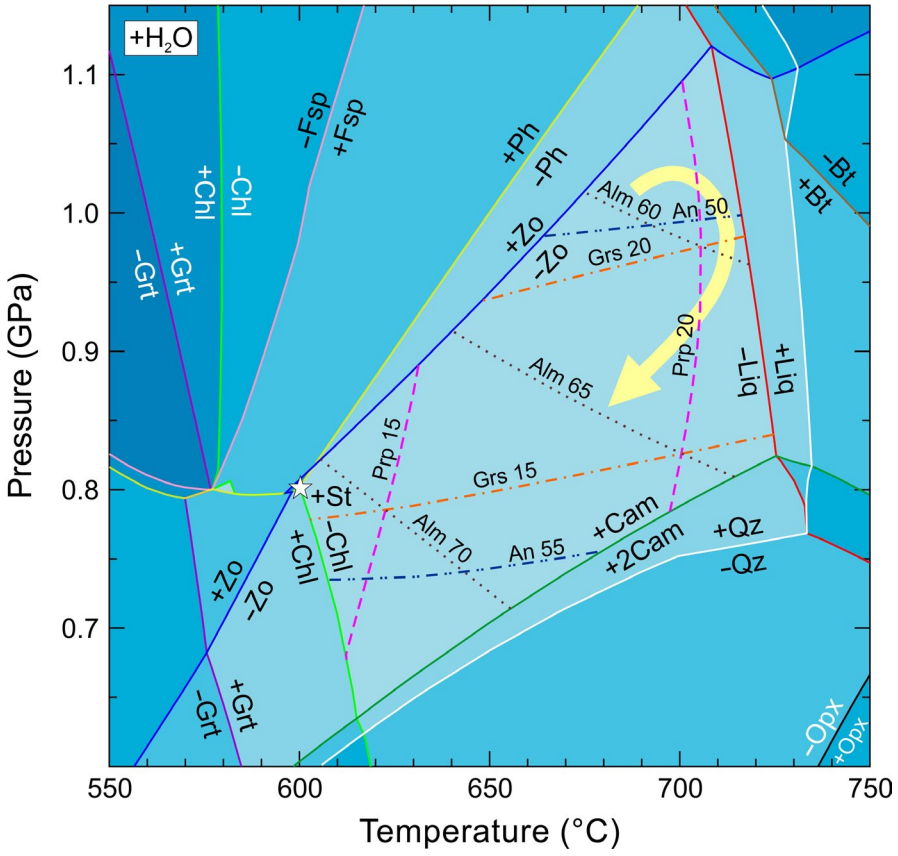

FIGURE 8 Equilibrium assemblage diagram for sample 86003 from Wirth (1989) calculated in the system NCKFMASH using the program Domino (de Capitani & Petrakakis, 2010) and the thermodynamic database of Holland and Powell (1998). The simplified bulk-rock composition in moles of 86003 is Si(46.99), Al(23.44), Fe(8.52), Mg(7.31), Ca(8.24), Na(4.66), K(0.86) and O(155.95). The modelling has used water in excess. The assemblage garnet–clinoamphibole–biotite–plagioclase–quartz is stable in the light-coloured area in the centre of the diagram. The asterisk marks a tiny staurolite stability field. Isopleths for grossular (Grs), pyrope (Prp), almandine (Alm) and anorthite (An) are labelled with contents in mol.%. The arrow shows the *P*–*T* path along which the model predicts the compositional trends found in garnet and plagioclase. Mineral abbreviations are from Whitney and Evans (2010)

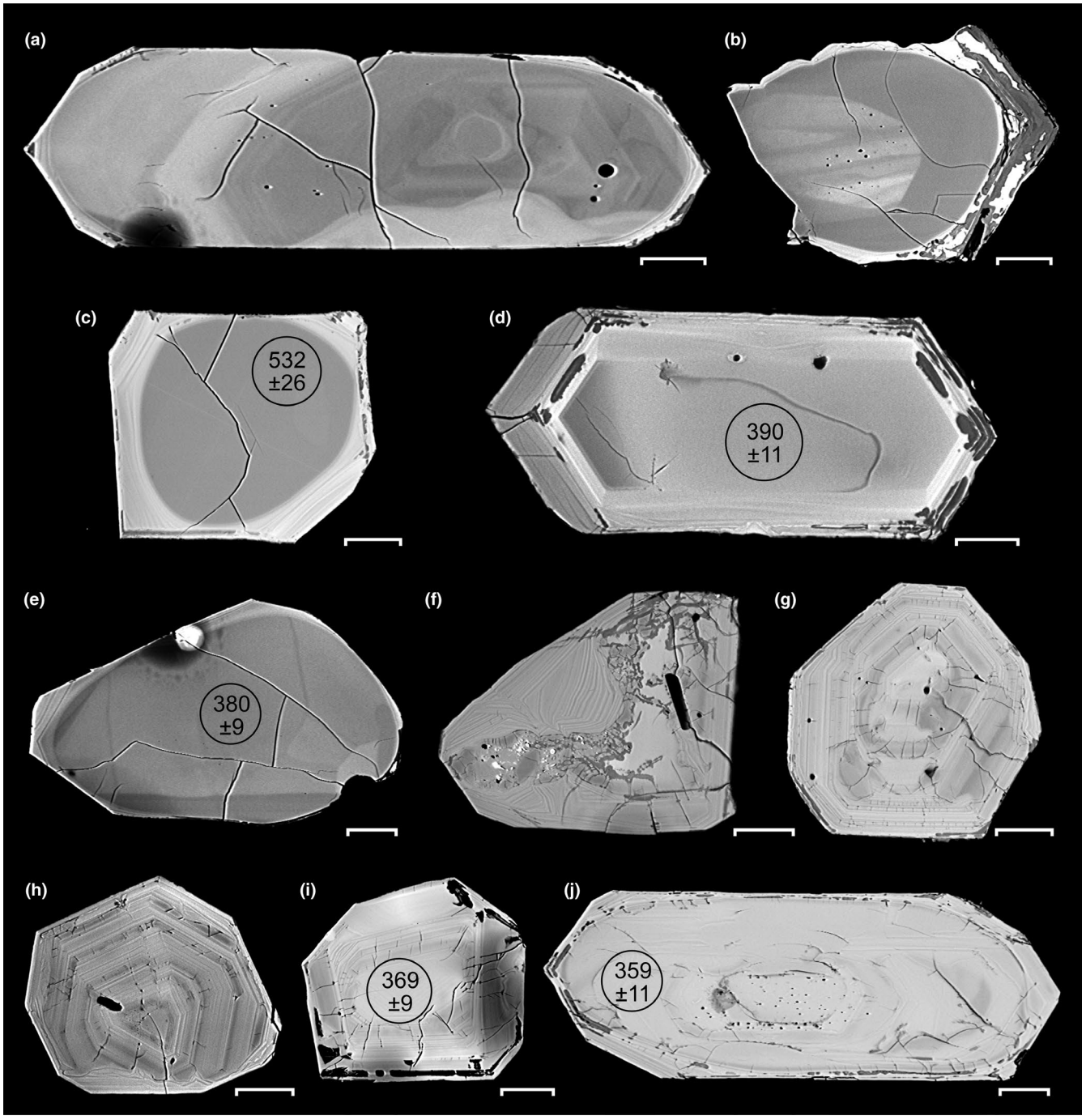

FIGURE 9 BSE images of zircons from sample Steina1: (a) A prismatic core with indistinct, concentric or sector zoning (Zrn1) is bounded on the left and lower sides by widely zoned, transgressive zircon, in turn overgrown by a finely zoned euhedral rim; grain no. 2. (b) An intermediate zone of homogeneous BSE-dark zircon (Zrn2) enclosing a planar-zoned multi-faceted core (Zrn1) has smoothly rounded interfaces with a finely zoned, altered rim; grain no. 16. (c) Finely zoned BSE-bright overgrowth (Zrn4) envelops a homogeneous, rounded, BSE-dark core (Zrn2); grain no. 4. (d) Prismatic crystal composed of homogeneous interior (Zrn3) and finely zoned concordant rims; grain no. 14. (e) Finely zoned overgrowth mantles an unzoned rounded core (Zrn3); grain no. 8. (f) A dissolution–reprecipitation reaction front propagating through homogeneous zircon produced the finely zoned zircon most common in sample Steina1; grain no. 17. (g) Patchy areas of homogeneous zircon persist in the core of a finely zoned euhedral crystal (Zrn4); grain no. 15. (h) A euhedral crystal (Zrn4) displays fine concentric zoning truncated by an overgrowth rim; grain no. 29. (i-j) Outer zones of euhedral crystals (Zrn4) and overgrowths are finely zoned, as opposed to absent or weak zoning in the core; grains no. 3 and 7. The circles show the location of laser spot analyses with concordant or near-concordant $^{206}Pb/^{238}U$ ages and 2σ error limits in million years. The dark and bright spots at grain margins in (a) and (e) are charging artefacts. Scale bar is 20 μm

TABLE 1 U–Th–Pb data for concordant to near-concordant zircons analysed by LA-ICP-MS from the samples Steina1 and 359/186b

Sample	Concentrations				Isotopic ratios							Isotopic ages						
Spot	Pb (ppm)	Th (ppm)	U (ppm)	Th/U	$^{206}Pb/^{204}Pb$	$^{207}Pb/^{206}Pb$	2σ (%)	$^{207}Pb/^{235}U$	2σ (%)	$^{206}Pb/^{238}U$	2σ (%)	$^{207}Pb/^{206}Pb$	2σ (Ma)	$^{207}Pb/^{235}U$	2σ (Ma)	$^{206}Pb/^{238}U$	2σ (Ma)	Cc. (%)
Steina1																		
01-012	152.4	3,721.8	2,061.9	1.81	3,270	0.05519	2.8	0.43763	3.9	0.05751	2.7	420.1	63.8	366.8	12.1	358.5	9.4	85
03-017	108.2	2,193.3	1,511.9	1.45	2,619	0.05391	3.4	0.44606	4.2	0.06001	2.5	367.5	78.5	368.5	13.1	368.6	9.0	100
04-019[a]	6.8	38.1	103.2	0.37	571	0.05900	10.8	0.68244	11.9	0.08389	5.1	567.0	254.3	538.7	51.0	532.0	26.1	94
04-020	14.5	44.3	273.8	0.16	831	0.05560	7.2	0.45062	7.7	0.05878	2.8	436.4	168.8	380.6	24.7	371.5	10.1	85
07-027	87.1	91.4	1641.4	0.06	7,189	0.05370	4.4	0.41663	5.4	0.05627	3.1	358.5	102.5	359.0	16.5	359.1	10.8	100
08-033	39.4	75.6	744.7	0.10	1,065	0.05425	4.7	0.45950	5.3	0.06143	2.5	381.4	109.2	379.9	16.9	379.7	9.2	100
14-051	147.4	1,126.3	2,269.5	0.50	5,220	0.05543	4.4	0.47079	5.3	0.06160	3.0	429.6	101.2	395.3	17.5	389.5	11.3	91
359/186b																		
02-013	5.7	70.6	61.5	1.15	260	0.06879	11.6	1.37406	12.0	0.14487	3.0	892.4	259.9	889.7	73.7	888.6	25.0	100
05-019	23.1	65.9	54.4	1.21	494	0.10969	4.7	5.25833	5.4	0.34768	2.6	1794.3	88.2	1858.6	47.1	1916.8	43.3	107
05-020	42.2	100.9	112.9	0.89	1,697	0.11160	4.1	5.09985	4.8	0.33143	2.5	1825.8	76.3	1,830.2	41.5	1834.1	40.0	100
08-025	28.9	129.1	308.2	0.42	1,042	0.06291	4.6	0.90635	5.1	0.10449	2.2	705.2	101.0	655.1	24.9	640.7	13.4	91
11-031	39.5	80.3	99.1	0.81	1,428	0.11187	4.6	4.99589	5.3	0.32389	2.7	1,830.1	85.8	1834.4	46.0	1838.3	43.3	100
17–043	32.4	401.3	304.6	1.32	397	0.06025	5.4	0.82973	6.1	0.09988	2.8	612.8	121.2	616.9	28.6	618.1	16.5	101
20-044	27.7	295.1	302.5	0.98	892	0.05641	6.1	0.59632	6.7	0.07667	2.8	468.5	141.1	470.3	25.5	470.6	12.7	100
20-045	38.5	613.2	535.5	1.15	407	0.05480	6.3	0.49030	6.6	0.06489	2.0	404.0	147.6	408.6	22.4	409.4	7.9	101
23-056	11.4	98.7	191.9	0.51	374	0.05433	9.0	0.44984	9.6	0.06005	3.2	384.7	216.0	383.1	31.1	382.8	11.9	100
29-068	36.9	276.7	286.2	0.97	996	0.06305	5.4	0.95722	6.3	0.11011	3.3	710.1	119.2	705.3	32.5	703.8	22.0	99

Note: cc.—Concordance level calculated as ($^{206}Pb/^{238}U$ age/$^{207}Pb/^{206}Pb$ age) × 100.

[a]Subslice representing the end of the time-resolved laser ablation spectrum.

being on the order of some percent too low for pyrope and too high for almandine compared with the analysis. One reason to explain this may lie in the neglect of TiO_2 in the simplified bulk-rock composition, which raises the amount of FeO distributed to minerals other than ilmenite. The finely layered texture of sample Krb1 defined by variation in the modal proportions of amphibole and plagioclase, with garnet-bearing layers abundant in plagioclase prevailing strongly over millimetre-scale amphibole-rich interlayers without garnet, is a second reason why the modelled bulk-rock composition may slightly deviate from that containing garnet. The modelling has also left out of account that the components locked inside zoned plagioclase have not equilibrated during peak metamorphism. De Capitani and Petrakakis (2010) inferred from analysed mineral compositions by comparison with those predicted by phase equilibria modelling that the latter generally show correct trends but are seldom precise.

8 | U-PB GEOCHRONOLOGY AND EVOLUTION OF ZIRCON

Zircon yield from the metagabbro sample Steina1 of the MSU and the metasediment sample 359/186b of the Schist Cover was low with only 35 and 26 grains retrieved from ~10 and ~5 kg samples, respectively, but was sufficient for LA-ICP-MS U-Pb dating. Two other metabasite samples from the MSU did not yield any zircon despite separation of up to 60 kg material.

The zircons of sample Steina1 are mostly brownish turbid, less commonly colourless transparent crystals of stout to short-prismatic habit, ranging in aspect ratio from 1.0 to 3.5. Internal structures reveal the presence of several zircon populations. Euhedral cores showing concentric, sector or banded zoning and locally resorbed crystal faces (Figure 9a,b) represent an early population (Zrn1). They occur within homogeneous, dark BSE zircon of the second population (Zrn2) that has rounded contacts with finely zoned, euhedral, light BSE overgrowths (Figure 9b,c). Such BSE-bright rims exist also on rounded grains of a third population (Zrn3) dated to be much younger than the second one (Figure 9e). The third population thus predates the BSE-bright overgrowths. It is characterized by euhedral crystals with homogeneous interior and finely zoned margins (Figure 9d), or by homogeneous rounded grains (Figure 9e). The population most common in sample Steina1 (Zrn4) consists of euhedral BSE-bright zircon with fine-scale concentric zoning throughout the crystals or in outer zones of crystals with blurred or absent zoning in the core (Figure 9g–j). The BSE-bright overgrowths and zircon formed by an arrested dissolution–reprecipitation reaction (Figure 9f) are in appearance similar to the fourth population, which may relate to this reaction, albeit a late dissolution–reprecipitation stage affected even this population, as is evident from narrow rims on embayed or rounded crystals (Figure 9h,j). Euhedral crystals containing polygonal inclusions of apatite, rutile, ilmenite and magnetite display internal structures that are mostly typical of the fourth population but do not exclude the third one. Magnetite, apatite, monazite, biotite, muscovite, chlorite, quartz and K-feldspar observed in irregularly shaped inclusions and pores of such crystals appear related to the metamorphism.

The zircon populations thus classified in sample Steina1 vary in trace element and U–Th–Pb isotopic composition. The U–Th–Pb concentrations determined by 60 spot analyses on 28 useable grains are generally low in the early two populations, dropping on average from 320 ppm U, 180 ppm Th and 20 ppm Pb in Zrn1 to an absolute low of 150 ppm U, 140 ppm Th and 10 ppm Pb in Zrn2, before rising to 1,030 ppm U, 640 ppm Th and 70 ppm Pb in Zrn3 and finally to 2,570 ppm U, 2,200 ppm Th and 170 ppm Pb in Zrn4. The Th/U ratios in Zrn1–Zrn3 range on average from 0.57 to 0.67, but rise to 0.95 in Zrn4, suggesting that the incorporation of Th relative to U increased strongly during late zircon growth. The rise in U content and the resulting radiogenic ^{206}Pb accumulation have caused an increase in the mean $^{206}Pb/^{204}Pb$ ratio from 360 to 370 in the early populations to 1,400–1,640 in the late populations (Appendix S8). High U contents are also the reason why Zrn4 has a brighter BSE signal.

Only 7 out of 60 zircon U–Pb isotopic data for sample Steina1 are concordant or near-concordant when using a 15% discordance cut-off (Appendix S8). All data for the first zircon population are discordant. The data for the second population include a $^{206}Pb/^{238}U$ age of 532 ± 26 Ma (2σ error) with a discordance degree of 6% (Table 1) generally accepted for geologically meaningful LA-ICP-MS U–Pb ages. Distinctly younger, concordant $^{206}Pb/^{238}U$ ages dating population 3 at 380 ± 9 Ma and population 4 between 369 ± 9 Ma and 359 ± 11 Ma agree within error with near-concordant $^{206}Pb/^{238}U$ ages for these populations (Table 1). The ages of the populations 3 and 4 are only partially within error of each other, suggesting formation of these populations during separate mid- and late-Devonian events. The weighted mean age for population 3 is 384 ± 7 Ma, and for population 4 is 365 ± 5 Ma, with an MSWD of 1.8 for both ages. The discordant data do not follow a single linear array, but define an almost continuous cluster with apparent $^{206}Pb/^{238}U$ ages largely within the age range of the concordant to near-concordant data (Figure 10).

The REE patterns of the zircon populations in sample Steina1 (Figure 11) show weak negative Ce and significant negative Eu anomalies in population 1 ($Ce/Ce^* = 0.62$, $Eu/Eu^* = 0.06$), compared to significant positive Ce and less negative Eu anomalies in population 2 ($Ce/Ce^* = 4.29$, $Eu/Eu^* = 0.33$) and in populations 3 to 4 (mean $Ce/Ce^* = 2.80$–3.05, mean $Eu/Eu^* = 0.29$–0.35). In general, Ce and Eu anomalies in zircon indicate the redox-sensitive substitution

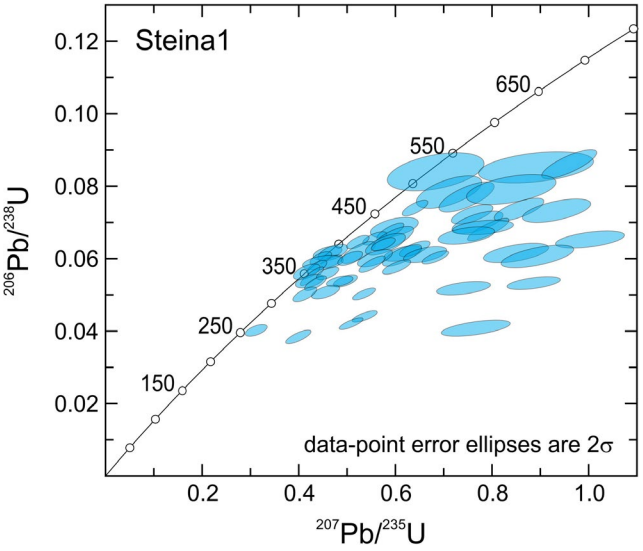

FIGURE 10 U–Pb concordia diagram for LA-ICP-MS zircon analyses from the metagabbro sample Steina1. Three discordant data with $^{207}Pb/^{235}U > 1.1$ are not shown

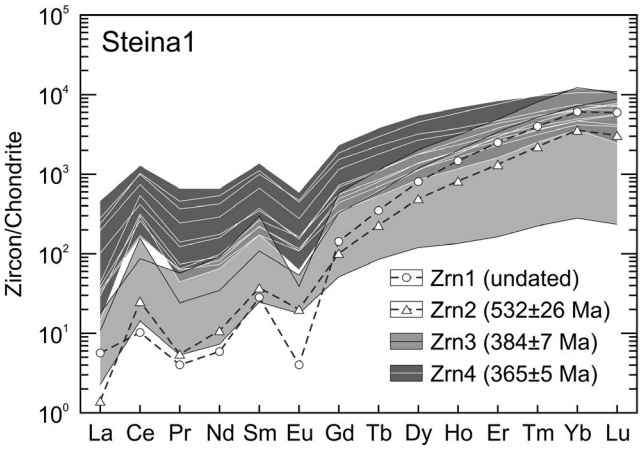

FIGURE 11 Rare earth element contents of zircons from sample Steina1 normalized to chondrite using the values from McDonough and Sun (1995). Dashed heavy lines denote zircons with concordant or near-concordant U–Pb ages

of these elements because, in addition to a trivalent state encountered for all lanthanides, Ce exists as zircon-compatible Ce^{4+}, and Eu as zircon-incompatible Eu^{2+} (Trail, Watson, & Tailby, 2012). The transition from negative to positive Ce anomalies, and from strong negative to less negative Eu anomalies between population 1 and populations 2–4 thus suggests a rise in oxidation state, with resulting higher Ce^{4+}/Ce^{3+} and Eu^{3+}/Eu^{2+} ratios in the reservoir from which the zircon grew. The trend in the total REE content is bimodal, with a first peak at 1,960 ppm in population 1, followed by a low at 1,140 ppm in population 2, before increasing to average contents of 2,330 ppm in population 3 and 3,550 ppm in population 4 (Appendix S9). The concentration gap between the populations is wider for the light and middle than the heavy REE (Figure 11). Belousova, Griffin, O'Reilly, and Fisher (2002) underlined that the average REE content in igneous zircons correlates with rock type and crystallization environment. They noted that the zircon REE contents in mafic igneous rocks typically vary between several hundred and 1,000 ppm, rarely up to 2,000 ppm, whereas those in granitoids and pegmatites can range up to percent levels, but admitted that high concentrations of the light REE and other trace elements can build up during secondary alteration. The zircon REE contents in sample Steina1 thus support a mafic igneous origin of Zrn2, and a metamorphic origin of Zrn3 and Zrn4.

The Ti concentrations in 23 zircon grains of sample Steina1 measured at 31 spots are partially below the detection limit of 25 ppm obtained with the electron microprobe. The 14 data above the detection limit range up to 93 ppm, with one outlier at 323 ppm, and comprise most data for Zrn1, the only data for Zrn2 and 35%–40% of the data for Zrn3 and Zrn4. Based on Ti-in-zircon thermometry (Ferry & Watson, 2007) and unit activity of SiO_2 and TiO_2, zircon Ti contents below 25 ppm impose an upper limit of 840°C on the crystallization temperature, which is consistent with zircon growth or recrystallization during metamorphism in the MSU. The higher Ti contents correspond to apparent temperatures in the range 840–915°C, but one analysis of Zrn1 and the only analysis of Zrn2 suggest crystallization temperatures near 1,000°C. The aberrant Ti content in one grain of Zrn4 may result from contamination by a mineral inclusion (Appendix S10). When formulating the Ti-in-zircon thermometer, Ferry and Watson (2007) took into account maximum plausible uncertainties that unconstrained activities of SiO_2 and TiO_2 can introduce into the calculation, assuming that the activity of TiO_2 in silicic melts at appropriate magmatic temperatures is rarely below 0.5, as is the activity of SiO_2 in most crustal rocks. The formulation therefore yields a temperature range corresponding to the maximum uncertainty that temperature underestimation at $aTiO_2 < 1$ or overestimation at $aSiO_2 < 1$ can cause. The temperatures designated as T_{min} and T_{max} in Appendix S10 indicate the related uncertainty, which does not include a slight pressure dependence of the thermometer that raises the temperature by ~50°C/GPa at pressures below the 1 GPa pressure of calibration.

The rounded to short prismatic detrital zircons in quartz–mica schist 359/186b of the Schist Cover enclose quartz, K-feldspar and apatite and have pores filled with albite and sodic muscovite. Oscillatory zoning and inherited cores are common, whereas a patchy internal structure and overgrowth rims are rare (Figure 12). The analysis of 23 useable grains by LA-ICP-MS has yielded 46 U–Th–Pb data, including 10 data with discordance below 10% and ages in the Late Palaeoproterozoic, Neoproterozoic, Ordovician and Devonian

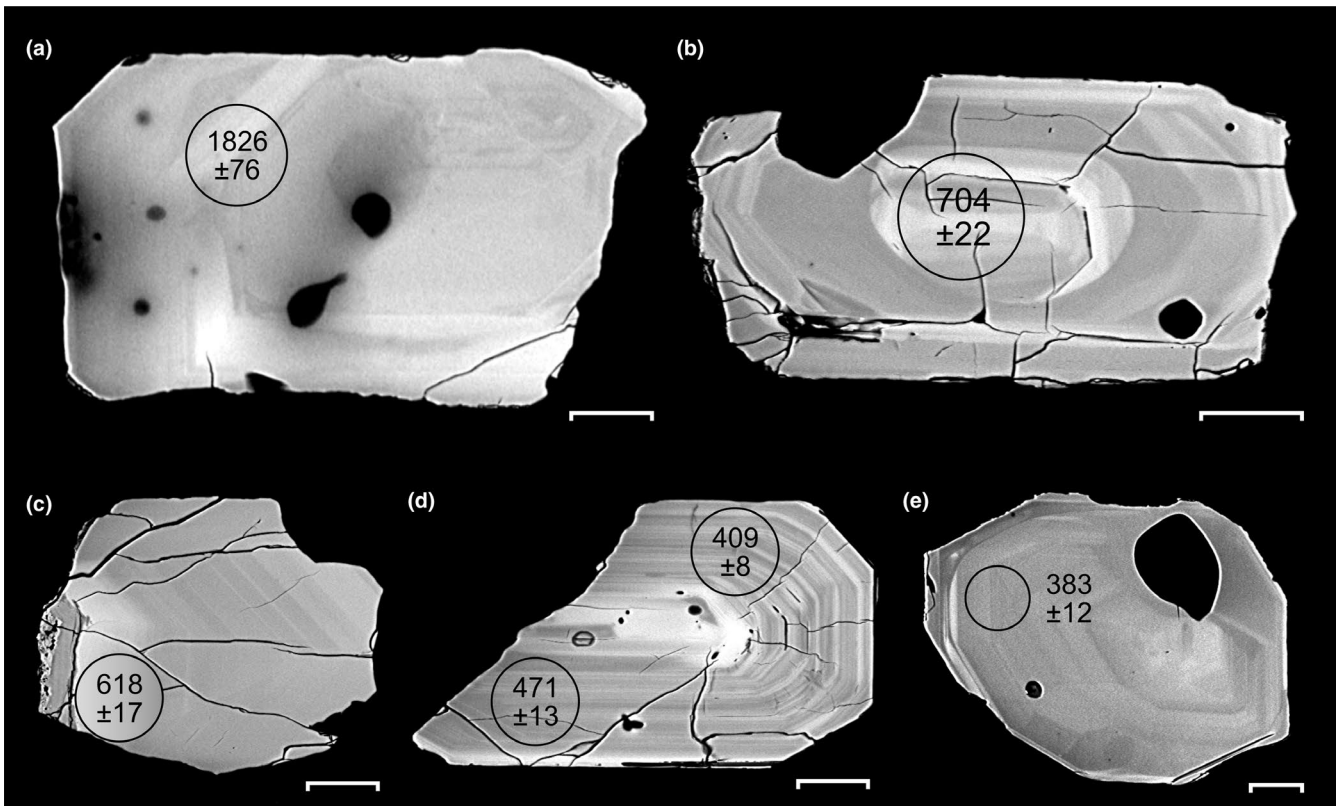

FIGURE 12 BSE images of detrital zircons from sample 359/186b labelled with locations of laser spots (circles) and resulting concordant $^{207}Pb/^{206}Pb$ (>1 Ga) or $^{206}Pb/^{238}U$ (<1 Ga) ages and 2σ error limits in million years: (a) Fragment with indistinct or absent zoning; grain no. 5. (b) A wide oscillatory-zoned grain contains an hourglass-zoned rounded core; grain no. 29. (c) Fragment with weak zoning; grain no. 17. (d) Broken prismatic crystal characterized by fine oscillatory zoning; grain no. 20. (e) Slightly abraded euhedral crystal with wide oscillatory zoning; grain no. 23. Scale bar is 20 μm

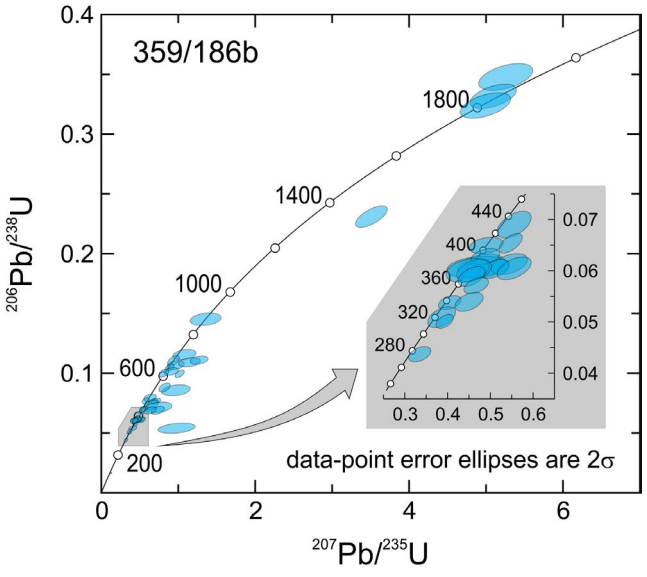

FIGURE 13 U-Pb concordia diagram for LA-ICP-MS analyses of detrital zircons from the metasediment sample 359/186b

(Appendix S8). The youngest concordant zircon constrains the protolith age of the metasedimentary rock to younger than 383 ± 12 Ma (Table 1). The concordia plot shows that the discordant data fall mostly close to the concordant ones, except for a few discordant zircons with young apparent ages indicating isotopic disturbances in post-Devonian times (Figure 13). The average U-Th contents increase systematically from 90 ppm U and 80 ppm Th in Palaeoproterozoic zircons to ~360 ppm of both U and Th in Devonian zircons, with a concomitant decrease in Pb content from 35 to 25 ppm, and in $^{206}Pb/^{204}Pb$ ratio from 1,210 to 390.

9 | Ar–Ar GEOCHRONOLOGY

Ar–Ar amphibole dating of metagabbro Böh2 from the MSU has yielded different ages for the grain size fractions 170–250 μm and 250–500 μm. The coarser-grained amphibole (Amp1) has a weighted mean age of 341 ± 2 Ma (97% of ^{39}Ar) and the finer one (Amp2) a weighted mean age of 328 ± 8 Ma (79% of ^{39}Ar) that is less precise due to a lower potassium content (Ca/K ratio ~100). Generally, the variation in amphibole composition observed within samples (Figure 4) is too low to induce significant differences in argon retention. Amphibole from garnet amphibolite Krb1 of the MSU closed to argon diffusion 334 ± 1 Ma and is, within error, the same age as the fine amphibole from sample Böh2.

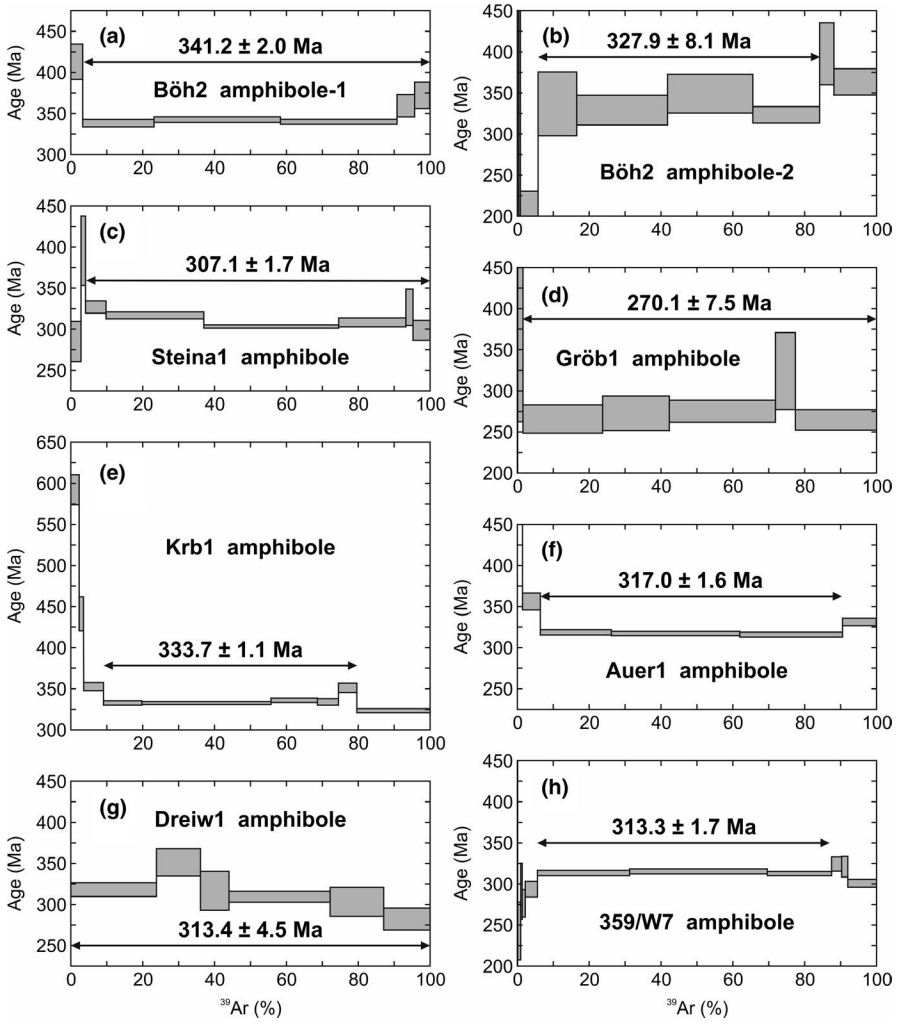

FIGURE 14 $^{40}Ar/^{39}Ar$ age spectra of amphibole from (a–f) Metagabbro/Serpentinite Unit, (g) Cordierite-Gneiss Unit and (h) Schist Cover of the Saxon Granulite Massif. All errors are 1σ

In four other metabasites (Dreiw1, Auer1, Steina1 and 359/W7) that represent all three upper units of the SGM, Ar retention began only in the period from 317 to 307 Ma. A notably young Ar–Ar plateau age dates the closure to Ar diffusion in amphibole from mylonitic amphibolite Gröb1 of the MSU to 270 ± 8 Ma. Figure 14 shows the amphibole age spectra documented in Appendix S11. Table 2 summarizes the Ar–Ar step heating results.

The observed intra-sample variation in composition of biotite and white mica (Figures 5 and 6) is negligible with respect to the closure of these minerals to argon loss. The Ar–Ar biotite plateau ages obtained from felsic and mafic granulites and intrusive granite in the granulite body and, higher in the section, from metasedimentary rocks in the Cordierite-Gneiss Unit and the Schist Cover do not correlate with composition, grain size or texture, nor do they continuously decrease from the flanks to the core of the massif, as would be expected from cooling of the exhumed hot granulite body in the upper crust (Figure 15, Table 2). Instead, they reveal an inverse younging direction in the roof of the massif, where the ages decrease from 327 ± 1 Ma a short distance above the granulite contact (samples 10/07-10 and Tr3) to 324–323 Ma higher up in the Schist Cover (samples 10/07-15 and G97-7). The oldest Ar–Ar biotite age, 335 ± 1 Ma, comes from a granite dyke in the granulite body (sample St1) and is indistinguishable, within error, from zircon ages of other late-kinematic granite bodies in the SGM (Figure 2). Figure 16 depicts the mica age spectra for which Appendix S12 provides the analytical data.

10 | DISCUSSION

10.1 | Plate affinity and protoliths

Sagawe et al. (2016) calculated a few Palaeoproterozoic but mainly Mesoproterozoic zircon Hf model ages for three samples of Saxon granulites and inferred an affinity to southern Baltica, with minor admixture of peri-Gondwanan or West African material during Variscan collision. Recalculation of these model ages using the whole-rock $^{176}Lu/^{177}Hf$ values rather than a fixed continental crust value, as suggested by Bea et al. (2018), slightly elevates the model ages for two of the samples. The Lu-Hf concentrations given for another

TABLE 2 Summary of $^{40}Ar/^{39}Ar$ step-heating ages. ^{39}Ar (%) is the relative amount of released ^{39}Ar used to calculate the plateau and weighted-mean ages (1σ error limits)

Unit	Sample	Rock type	Mineral	Grain size (μm)	No. of gas fractions	% ^{39}Ar	Plateau/weighted-mean age (Ma)	Inverse isotope correlation age (Ma)	Isotope correlation age (Ma)	Total gas age (Ma)
Schist cover	G97-7	Qz-mica schist	Ms	250–500	3	85.7	306.5 ± 1.7	na	na	323.5 ± 2.4
	359/W7	Amphibolite	Amp	250–500	3	82.1	313.3 ± 1.7	311.7 ± 3.5	313.2 ± 3.5	311.5 ± 1.7
	G97-7	Qz-mica schist	Bt	170–500	6	72.8	322.7 ± 1.3	na	na	315.9 ± 1.4
	10/07-15	Quartzite	Ms	250–500	7	92.3	324.4 ± 0.9	324.5 ± 1.7	324.8 ± 1.6	323.9 ± 0.8
	Tr3	Sil-Bt schist	Bt	250–500	8	67.7	327.3 ± 0.7	322.7 ± 2.9	328.0 ± 2.0	325.2 ± 0.6
MSU	Gröb1	Amphibolite	Amp	170–250	5	98.5	270.1 ± 7.5	266.3 ± 13.3	280.2 ± 53.8	275.1 ± 9.0
	Steina1	Metagabbro	Amp	170–250	6	92.7	307.1 ± 1.7	na	na	310.0 ± 2.2
	Auer1	Grt amphibolite	Amp	170–250	3	84.3	317.0 ± 1.6	317.1 ± 5.2	nc	327.6 ± 1.8
	Böh2	Metagabbro	Amp2	170–250	4	78.6	327.9 ± 8.1	na	na	337.1 ± 10.2
	Krb1	Grt amphibolite	Amp	170–250	5	70.6	333.7 ± 1.1	331.9 ± 2.3	337.0 ± 2.1	341.0 ± 1.0
	Böh2	Metagabbro	Amp1	250–500	5	96.8	341.2 ± 2.0	na	na	345.0 ± 2.3
CGU	Dreiw1	Amphibole fels	Amp	250–500	6	97.0	313.4 ± 4.5	na	na	322.5 ± 7.0
	10/07-10	Bt-Grt-Sil gneiss	Bt	250–500	10	97.0	326.8 ± 0.6	327.5 ± 1.6	326.6 ± 1.6	325.1 ± 0.5
Granulite complex	10/07-1A	Prm granulite	Bt	250–500	10	98.5	327.4 ± 0.6	327.0 ± 1.6	327.6 ± 1.6	327.3 ± 0.5
	Rt2	Mafic granulite	Bt	170–250	9	99.2	330.4 ± 0.6	330.1 ± 1.6	330.8 ± 1.6	329.4 ± 0.6
	St3	Felsic granulite	Bt	170–250	7	86.9	331.5 ± 0.8	331.8 ± 1.7	331.3 ± 1.7	328.1 ± 0.7
	Wh2	Felsic granulite	Bt	170–250	5	59.9	331.8 ± 1.3	326.7 ± 5.8	331.4 ± 6.6	328.5 ± 1.2
	Wh4	Crn granulite	Bt	250–500	5	52.9	332.4 ± 1.2	328.7 ± 2.9	332.6 ± 3.5	330.0 ± 0.9
	St1	Granite dyke	Bt	250–500	5	67.3	334.9 ± 1.0	na	335.2 ± 2.8	325.0 ± 3.1

Note: Plateau age criteria are from Fleck, Sutter, and Elliot (1977), mineral abbreviations from Whitney and Evans (2010).

Other abbreviations: MSU—Metagabbro/Serpentinite Unit; CGU—Cordierite-Gneiss Unit; na—does not apply for weighted-mean ages; nc—no correlation.

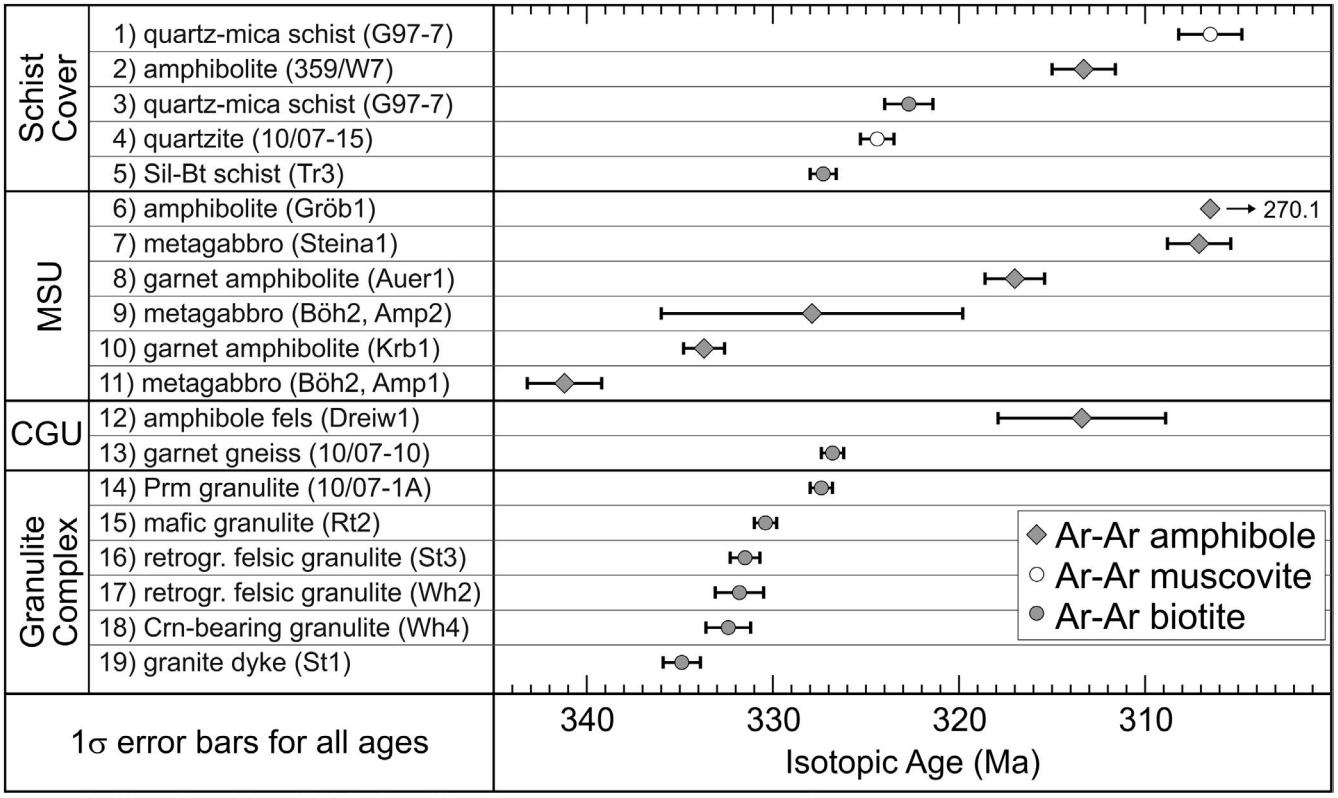

FIGURE 15 Ar–Ar amphibole and mica ages determined in this study, with listing from top to bottom in order of increasing age within the structural units of the Saxon Granulite Massif. The Metagabbro/Serpentinite Unit and the Cordierite-Gneiss Unit are abbreviated as MSU and CGU, respectively. For the Rb–Sr muscovite age of sample G97-7, see Figure 2

sample (G10) translate into a $^{176}Lu/^{177}Hf$ value two times as high as the present-day chondrite value, thus cautioning against the effect of analytical error on this method.

The interpretation calls for a comparison between the εHf-time arrays of the Saxon granulites and potential source areas. Southern Baltica and Avalonia share a common two-stage Lu–Hf evolution. An early trend towards more radiogenic zircon εHf values suggests oceanic crust accretion during Archean to mid-Mesoproterozoic continental growth. This trend reversed during Grenvillian-age crustal reworking. The evidence for Avalonia comes from detrital zircon data indicating that an unexposed continental basement with affinity to Baltica underlies mid- to late-Neoproterozoic oceanic arc successions. Late Neoproterozoic zircons with highly variable εHf values record a third stage in the Hf evolution of Avalonia related to mixing of radiogenic oceanic arc crust with unradiogenic reworked material from the underlying Baltic basement and the docking margin of Gondwana (Henderson, Collins, Murphy, Gutierrez-Alonso, & Handa, 2016; Spencer, Kirkland, Prave, Strachan, & Pease, 2019). It is uncertain whether Avalonia lay off the South American or West African part of Gondwana during Ediacaran-Cambrian time (Cambeses, Scarrow, Montero, Lázaro, & Bea, 2017; Cocks & Fortey, 2009; Henderson et al., 2016). After separation from Gondwana and assembly with Laurentia and Baltica into Laurussia, Avalonia came in contact, and southern Baltica in proximity, to northern Gondwana during the Variscan orogeny that extended into Avalonia, but did not affect Baltica inside Laurussia (Figure 1).

The Saxon granulites have εHf(t) values from −15.8 to 0.6 for late Neoproterozoic to early Palaeozoic inherited and protolith zircons, and values in the upper part of this range for the predominant Variscan metamorphic zircons. The only outlier is a concordant zircon core, dated at *c*. 2.1 Ga, with radiogenic εHf(t) of 2.4 (Sagawe et al., 2016). This εHf-time array is distinct from those for Baltica and Avalonia by an age gap from the late Palaeoproterozoic to the early Neoproterozoic, whereas striking similarity exists with the age gap from 1.6 to 1.1 Ga in rocks of West African affinity (Linnemann, Gerdes, Drost, & Buschmann, 2007). We interpret the Palaeoproterozoic Hf isotopic signature of the Saxon granulites as due to crustal reworking of an old West African component, consistent with Palaeoproterozoic model ages for late Neoproterozoic to early Palaeozoic zircons (Figure 17a,b). The wide scatter of εHf(t) in these zircons reflects mixing of isotopically evolved Palaeoproterozoic crust with juvenile late Neoproterozoic to early Palaeozoic components, with resulting geologically meaningless Mesoproterozoic mixing ages. Juvenile input into the northern Gondwana margin is actually evident in Ediacaran-Ordovician sequences of the

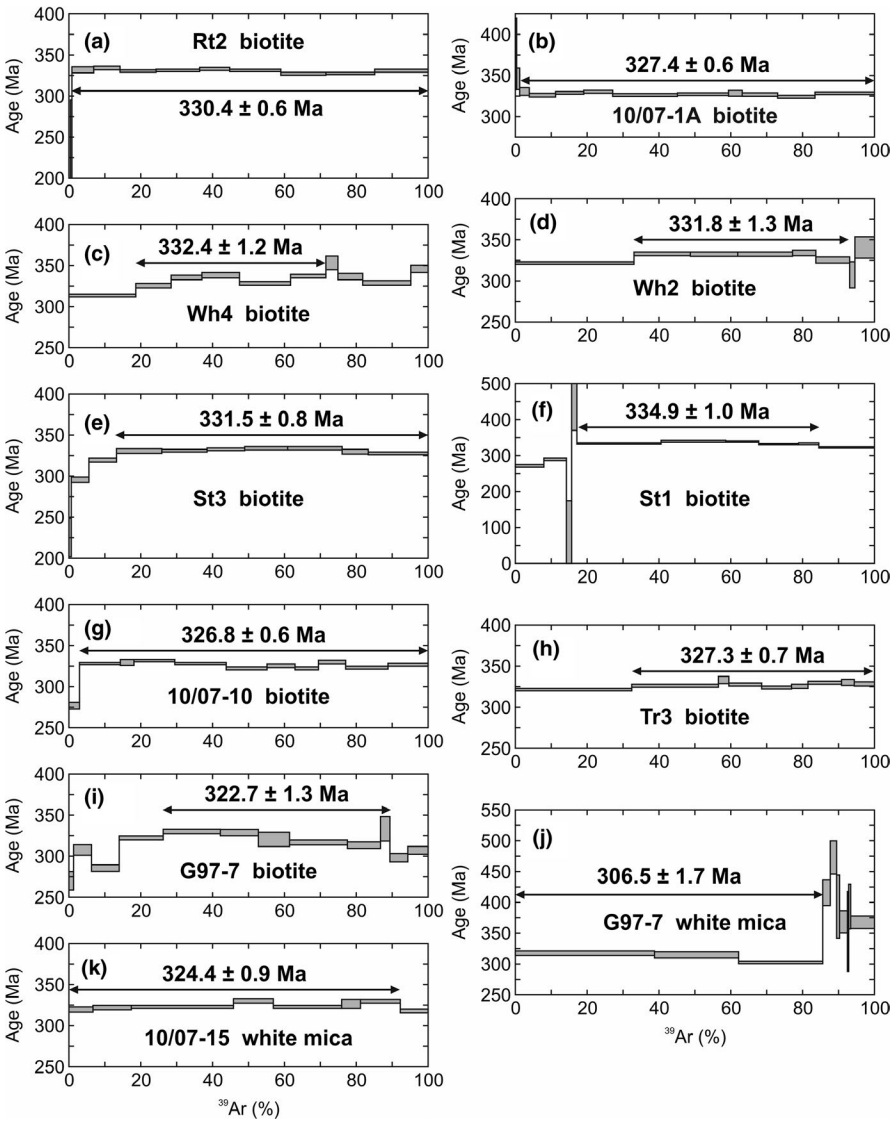

FIGURE 16 $^{40}Ar/^{39}Ar$ age spectra of biotite and white mica from (a–f) Granulite Complex, (g) Cordierite-Gneiss Unit and (h–k) Schist Cover of the Saxon Granulite Massif. All errors are 1σ

Saxothuringian belt and the Iberian Ossa-Morena Zone. These deposits generally have late Palaeoproterozoic Nd model ages but yield Mesoproterozoic Nd model ages in the early Cambrian of the Ossa-Morena Zone and in the late Ediacaran and late Cambrian of the Saxothuringian belt. The excursions in mean mantle extraction age indicate mixing between old crust and young juvenile material during the late Neoproterozoic active margin and the early Palaeozoic rift magmatism in northern Gondwana (Cambeses et al., 2017; Romer & Hahne, 2010). Feldspar Pb isotopic compositions support an affinity of the Saxon granulites to northern Gondwana by being less radiogenic in the internal Variscan Saxothuringian belt, including the SGM, than in the reworked Avalonian crust of the external Variscan Rhenohercynian belt (Jaeckel et al., 1999).

Kroner et al. (2007) have argued that the Saxothuringian crust did not comprise an oceanic realm, which is contrary to the assumption of early Palaeozoic ocean basin formation and seafloor spreading between microplates rifted off from the northern Gondwana margin (Cambeses et al., 2017; Franke, 2000; Schulmann et al., 2014). Palaeomagnetic data show that apart from the two major continental plates, Gondwana and Laurussia, microplates located in between collided during the Variscan orogeny (Tait, 1999). Such data led Schätz (2004) to infer that the Saxothuringian microplate drifted away from Gondwana in the mid-Ordovician some time after Avalonia had broken free in the Arenigian.

The Metagabbro/Serpentinite Unit of the SGM is an allochthonous unit exhumed in ductile contact with the underlying granulites. Lünser (1994) regarded it as a vestige of upper mantle and lower crust from a once coherent oceanic lithosphere section, with fragments of related oceanic upper crust occurring in the Frankenberg Klippe to the southeast of the SGM (see also Rötzler, Carswell, Gerstenberger, & Haase, 1999). She ascribed the relic magmatic two-pyroxene mineralogies of the metabasites to crystallization from fractionating tholeiitic magma. A classification of the metabasites using the basalt discriminant diagrams of Pearce

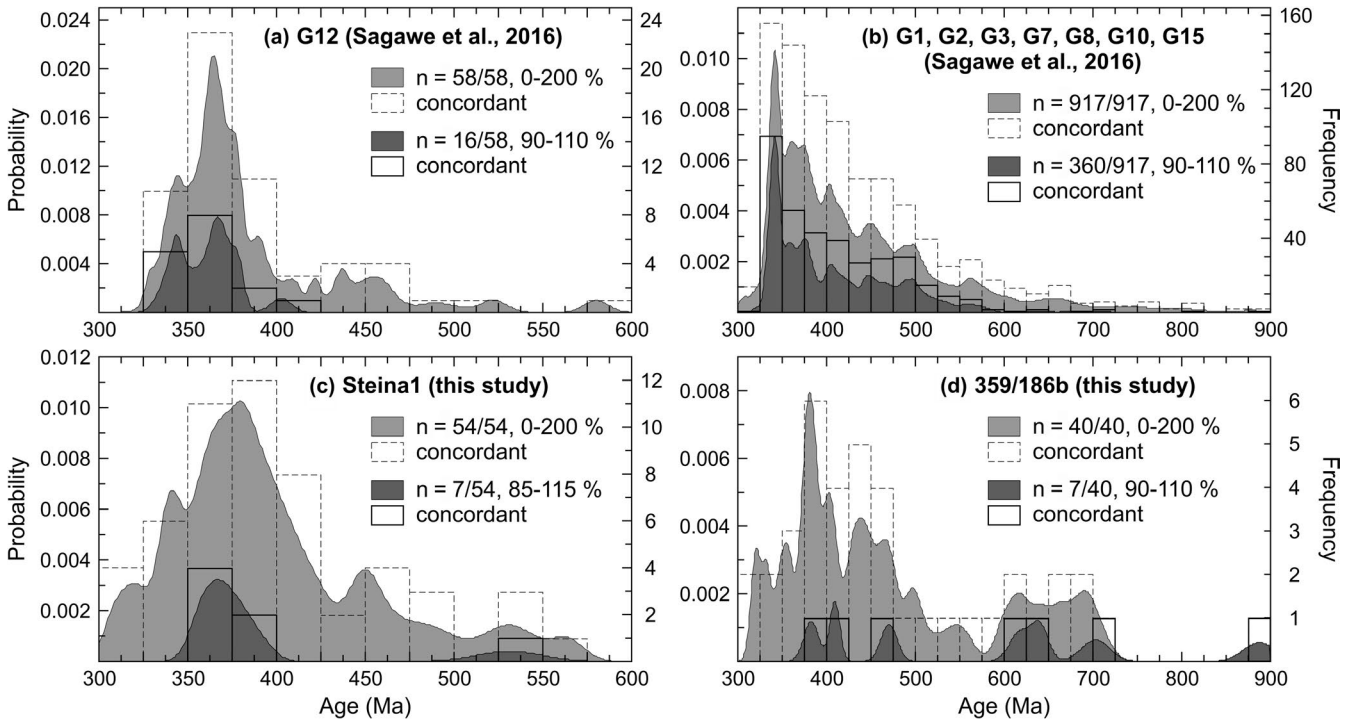

FIGURE 17 Combined age histograms and probability density distribution diagrams for zircon from (a) mafic granulite and (b) felsic granulite of the Saxon Granulite Massif analysed by Sagawe et al. (2016) in comparison to zircon from (c, d) the studied samples. Light shaded areas and dashed bins include all data in the given age range, dark shaded areas and solid bins only the concordant to near-concordant data. Six data from each (a), (c) and (d) and 25 data from (b) are out of the shown age range

(1976) assigns the mafic metagabbros to ocean floor basalt, the more felsic and cumulate metagabbros to calc-alkaline basalt, and the metadolerites to ocean floor basalt and low-K tholeiite. According to Lünser (1994), the harzburgitic–dunitic serpentinites represent the depleted suboceanic upper mantle, whereas the metabasites comprise stratified low-level cumulates (Ti-rich metagabbros), non-stratified high-level intrusives (mafic tholeiitic and more felsic calc-alkaline metagabbros) and sheeted dykes (metadolerites).

Zircon internal structures and U-Pb ages of herein studied metagabbro from the MSU show that zircon cores representing three distinct early populations escaped a late dissolution–reprecipitation process producing the predominant zircon population (Figure 9). Zircon relics that survived replacements within older zircon grains and/or overgrowth on older cores often do not provide enough concordant ages to make a statistical sample, thus requiring a cautious age interpretation. The zircon core age of 532 ± 26 Ma obtained from metagabbro is the true formation age of the second zircon population in sample Steina1, considering the low degree of discordance (6%). By taking into account the notably low U-Th-Pb concentrations in this zircon (Table 1) and their association with a low chondrite-normalized REE pattern (Figure 11), a low total REE content (Appendix S9), and a crystallization temperature near 1,000°C (Appendix S10), we interpret the Early Cambrian zircon age as the time of gabbro intrusion.

This interpretation fits well to the regional context of the MSU within the internal Variscan Saxothuringian belt in which different areas contain MORB-type rocks, generally of Cambro-Ordovician age (Gebauer & Grünenfelder, 1979; Kemnitz, Romer, & Oncken, 2002; Oliver, Corfu, & Krogh, 1993; Stosch & Lugmair, 1990; Tichomirowa & Köhler, 2013; Timmermann et al., 2004; Von Quadt & Günther, 1999). These oceanic vestiges are clearly older than those of Devonian age located in, or originating from, the external Variscan Rhenohercynian belt. Kryza and Pin (2010) therefore inferred that the vestiges of mature oceanic crust found in the Variscan belt relate to various continental break-up events at the northern Gondwana margin. An example of Devonian oceanic opening is the Lizard Complex of SW England, where rapid exhumation of lower crustal and mantle rocks occurred below a local pull-apart rather than an extensive along-strike ocean basin 397 ± 2 Ma. Metamorphism of lower crustal rocks due to juxtaposition with exhuming mantle rocks occurred between 393 ± 6 Ma and 386 ± 7 Ma, based on structureless or, rarely, sector or oscillatory-zoned zircons. Intra-oceanic thrusting of the exhumed rocks during oceanic closure preceded final emplacement onto mid-Devonian foredeep sediments at the margin of Avalonia (Clark, Scott, Sandeman, Bromley, & Farrar, 1998; Cook, Holdsworth, Styles, & Pearce, 2000; Nutman, Green, Cook, Styles, & Holdsworth, 2001). Another example, the Ślęża ophiolite of SW Poland, developed coevally with the

TABLE 3 Zircon saturation temperatures (T_{Zrn}) and saturation concentrations of Zr in melt at 1,000°C (C_{Zr}) for zircon-bearing MORB-type rocks from various parts of the Variscan belt calculated using the zircon solubility models of Watson and Harrison (1983) and Shao et al. (2019)

Author[a]	R&T	T&K	T&K	T&K	T&K	T&K	TSG	KEM	OLV	K&P
Rock type	Gabbro	Eclogite	Eclogite	Eclogite	Eclogite	Eclogite	Eclogite	Gabbro	Gabbro	Basalt
Sample	Steina1	Nau	Schm5	Rei	Ocar4	Ocar6	HT−99–09	VE9602	BM94	S5
Age[b]	532 ± 26	538 ± 3	541 ± 4	533 ± 4	539 ± 3	543 ± 6	539 ± 2	502 ± 2	494 ± 2	403 ± 6
Whole-rock chemistry (wt%)										
SiO_2	51.40	51.40	50.90	50.30	52.50	53.10	48.30	48.80	49.99	48.68
TiO_2	0.31	1.55	1.32	1.19	0.93	1.50	1.37	0.78	0.50	1.39
Al_2O_3	18.40	14.10	14.50	15.80	15.70	14.20	18.80	15.90	15.14	20.44
FeO_t	5.03	10.17	9.81	8.94	7.84	10.26	10.40	7.74	11.97	5.98
MnO	0.11	0.23	0.19	0.17	0.16	0.20	0.19	0.11	0.22	0.08
MgO	8.77	6.81	7.03	7.50	7.66	6.39	6.93	7.10	6.34	1.72
CaO	10.28	10.10	10.50	11.30	8.67	9.80	9.82	10.90	11.38	19.37
Na_2O	2.36	3.05	2.83	2.37	2.72	2.81	2.76	2.00	1.02	0.15
K_2O	0.55	0.50	0.69	0.26	0.76	0.49	0.12	1.40	0.09	0.00
P_2O_5	0.02	0.12	0.11	0.13	0.10	0.06	0.29	0.07	0.22	0.15
H_2O^+	1.89	n.a.	n.a.	n.a.	n.a.	n.a.	n.a.	n.a.	n.a.	n.a.
CO_2	0.11	n.a.	n.a.	n.a.	n.a.	n.a.	n.a.	n.a.	n.a.	n.a.
LOI	*n*.a.	0.51	0.38	0.26	1.48	0.07	n.a.	n.a.	2.23	1.74
Total	99.22	98.54	98.26	98.22	98.52	98.88	98.98	94.80	99.10	99.70
Zr (ppm)	28	87	89	89	75	74	87	54	21	91
Model	Watson and Harrison (1983)									
M[c]	2.62	3.47	3.49	3.28	2.69	3.22	2.64	3.25	3.03	3.65
T_{Zrn} (°C)	589	613	614	625	646	617	659	596	554	607
C_{Zr} (ppm)	3,498	7,230	7,361	6,150	3,711	5,824	3,571	6,001	4,947	8,409
Model	Shao et al. (2019)									
G[d]	2.71	2.33	2.31	2.35	2.64	2.47	2.52	2.44	2.35	2.98
T_{Zrn} (°C)	210	353	355	359	356	340	370	289	136	411
C_{Zr} (ppm)	4,748	5,831	5,897	5,750	4,924	5,386	5,234	5,491	5,774	4,184

Abbreviations: LOI, loss on ignition; n.a., not analysed.

[a]R&T—Rötzler and Timmerman (this study); T&K—Tichomirowa and Köhler (2013, eastern Erzgebirge, Germany); TSG—Timmermann et al. (2004, Mariánské Lázně Complex, Czechia); KEM—Kemnitz et al. (2002, Vesser area, Germany; whole-rock data from Bankwitz, Bankwitz, Kramer, & Pin, 1994, their sample 6807); OLV—Oliver et al. (1993, Rudawy Janowickie Mts., Poland; whole-rock data from Winchester, Floyd, Chocyk, Horbowy, and Kozdroj (1995), their sample PA-5); K&P—Kryza and Pin (2010, Ślęża ophiolite, Poland).

[b]Protolith zircon ages (Ma, ±2σ) obtained using ID-TIMS, SHRIMP or LA-ICP-MS U–Pb, or single-grain Pb–Pb evaporation techniques

[c]Bulk cationic (Na+K+2Ca)/(Al×Si) ratio.

[d]Bulk molar $(3Al_2O_3+SiO_2)/(Na_2O+K_2O+CaO+MgO+FeO)$ ratio.

Lizard Complex, albeit obviously in a wider ocean basin. U–Pb zircon ages for low-grade metabasalt and metagabbro indicate oceanic magmatism at 403 ± 6 Ma and 400 ± 10 Ma. Geochemical signatures combined with zircon fluid inclusion and U–Pb age evidence record mid-ocean ridge magmatism and deep-sea hydrothermal activity at 400 +4/−3 Ma. The occurrence of boninitic rodingites implies that seafloor alteration continued until the rocks had migrated from a mid-ocean ridge to a supra-subduction zone setting. Ophiolite detritus carried into platform sediments of likely late Frasnian, or at least Famennian, age provides a time constraint for the final emplacement of the ophiolite (Dubińska et al., 2004; Kryza & Pin, 2010; Muszer & Haydukiewicz, 2011).

The mid- to late-Devonian zircon ages in metagabbro of the MSU are consistent with metamorphic ages of oceanic rocks in the internal Variscan belt (Kreuzer et al., 1989; Stosch & Lugmair, 1990; Timmermann et al., 2004), but are not a good fit with the history of oceanic rocks in the external Variscan belt, such as the Lizard or Ślęża ophiolites. However, if we were to consider the early Cambrian zircon in

the MSU as inherited from the magma source, then the zircon dated at 384 ± 7 Ma could record gabbro formation synchronous with gabbro and dolerite intrusions into the exhuming Lizard peridotites (Cook et al., 2000), though such intrusions are unknown in the MSU serpentinites. Zircon growth in the MSU at 365 ± 5 Ma even postdates the final emplacement of the Lizard and Ślęża ophiolites (Cook, Holdsworth, & Styles, 2002; Kryza & Pin, 2010). Nevertheless, it is theoretically possible that the MSU originated by mid-Devonian oceanic magmatism while Cambro-Ordovician oceanic rocks now associated in the same region were subducted (Stosch & Lugmair, 1990; Timmermann et al., 2004). The metamorphism of the studied metagabbros would then have taken place during final oceanic closure in the late Devonian.

In view of these arguments, we henceforth consider the Early Cambrian zircon age in metagabbro Steina1 as the protolith age. Ti-in-zircon thermometry indicating crystallization of the protolith zircon at a temperature near 1,000°C agrees with two-pyroxene thermometry data recording magmatic crystallization of the MSU metabasites over the range 900–1,200°C, with higher estimates for the metagabbros than the metadolerites (Lünser, 1994). The zircon solubility models of Watson and Harrison (1983) and Shao, Xia, Ding, Cai, and Song (2019) when applied to MORB-type rocks from the Variscan belt, including sample Steina1, predict zircon saturation temperatures (Table 3) clearly below the wet MORB solidus at appropriate pressure conditions (Vielzeuf & Schmidt, 2001). Hence, the models preclude that zircon can precipitate from melts equivalent to these rocks, contrary to the invariably inferred presence of magmatic zircon. Several reasons may account for this discrepancy. Watson and Harrison (1983) restricted their model to melts lower in basicity than the mafic rocks considered here. Apart from the applicability range of this model, melts containing cumulus minerals differ in composition from the solidified rocks. In case of calcic cumulus clinopyroxene or amphibole, the model predictions based on whole-rock analyses overestimate the Zr concentration needed to saturate the melt in zircon and, conversely, underestimate the zircon saturation temperature (Janoušek, 2006). This seems to apply to the zircon-bearing MORB-type rocks listed in Table 3, whose Zr concentrations are roughly two orders of magnitude lower than those predicted at zircon saturation at 1,000°C in melts equivalent to these rocks. Watson and Harrison (1983) reported a strong decrease in zircon solubility with H_2O content in melts with <2 wt% H_2O. Shao et al. (2019) argued that not the solubility but the dissolution rate of zircon decreases in H_2O-deficient melts. Their solubility model considering also mafic melts predicts saturation concentrations of Zr that vary around those implied by Watson and Harrison's (1983) model (Table 3). The slow Zr diffusion in H_2O-deficient melts and the high ability of mafic melts to dissolve inherited or entrained zircon (Shao et al., 2019; Watson & Harrison, 1983) may lead to local saturation in zircon, in particular, if the melt cools faster than the Zr diffusion allows localized high concentrations of Zr to homogenize. Mafic melts with bulk Zr concentrations far below the zircon saturation threshold could thus precipitate zircon. Rapid growth of rock-forming minerals during in situ fractional crystallization of mafic melts does not only change the composition of, and reduce the zircon solubility in, the residual melt but may also induce disequilibrium concentration gradients of Zr around crystals unable to quantitatively take up the Zr content dissolved in melt, thus causing mesostasis growth of zircon in rocks with bulk Zr concentration levels below the saturation threshold (Bacon, 1989). The metabasites of the Ślęża ophiolite, owing to their weak deformation and metamorphism, exhibit well-preserved igneous textures (Oliver et al., 1993). The metagabbros are strongly depleted in incompatible elements and are associated with diffuse plagioclase-rich segregations locally coalescing into centimetre-scale, still partly diffuse, aplitic veins. Kryza and Pin (2010) inferred a co-genetic origin of the segregations with the cumulate gabbros in which the segregations may represent intercumulus zircon growth liquid. Consequently, if the zircon saturation models are correct and magmatic zircon is truly present in the MORB-type rocks compiled in Table 3, then the zircon growth liquid did not match the respective bulk rock composition.

Heuse et al. (1994, 2010) correlated metasediments from the upper part of the Schist Cover of the SGM with various Saxothuringian sedimentary deposits dated by palynology as Neoproterozoic and by U–Pb zircon chronology as Ediacaran. However, detrital zircon ages from our sample 359/186b preclude that the said metasediments are older than Middle/Upper Devonian boundary time (Figure 17d). We interpret these metasediments as Upper Devonian deposits of the right-way-up sequence in the Schist Cover, in agreement with carbon isotope stratigraphy supporting a Palaeozoic rather than Neoproterozoic sedimentary age (Lorenz & Nitzsche, 2000). The occurrence of Palaeo- and Neo- but not Mesoproterozoic detrital zircons in these metasediments hints at West African and peri-Gondwanan provenances.

10.2 | Metamorphic evolution

Our results cast new light on the tectono-stratigraphy of the SGM by disclosing that the MSU differs not only in its oceanic affinity but also in its metamorphic history from the associated continental-crust units. Calculated phase equilibria and mineral composition isopleths when compared to the peak mineral assemblage in garnet amphibolite reveal a clockwise *P–T* path of the MSU that culminated in high-*P* amphibolite facies conditions slightly above 1.0 GPa and 700°C (Figure 8). Among the zircon populations found in metagabbro Steina1 of the MSU (Figure 9), metamorphic

populations are most common and are easy to distinguish from the older populations by their internal structures, mineral inclusions, higher U–Th–Pb contents, enrichment in light to middle REE, lower Ti concentrations, and much younger U–Pb ages. The metamorphic populations encompass unzoned and finely oscillatory-zoned zircon with weighted mean ages of 384 ± 7 Ma and 365 ± 5 Ma, respectively. These ages are outside error of each other, suggesting crystallization stages in the mid- and late-Devonian. Considering the progressive mylonitization and recrystallization of the protoliths with release of U, Th and REE from decomposing igneous minerals on the one hand, and the rise in the U–Th–Pb and REE concentrations between the metamorphic populations as well as the fluid-assisted dissolution–reprecipitation process that created the predominant population of metamorphic zircon on the other hand, we interpret the metamorphic zircon populations as products of near-peak and retrograde metamorphism. The elevated Th/U ratio and the less negative Eu anomaly in the retrograde metamorphic zircon population imply higher redox conditions with increasing oxidation of U^{4+} to less zircon-compatible U^{6+} (see Rioux et al., 2015), and of Eu^{2+} to Eu^{3+} that partitions preferentially into zircon. An unzoned zircon core with a U–Pb age of 380 ± 9 Ma represents the near-peak metamorphic population but has U, Th and REE concentrations rather similar to those of the protolith zircon (Table 1, Appendix S9) from which the trace element composition seems to be inherited (see Goodge, Fanning, & Bennett, 2001; Kryza & Fanning, 2007). In both metamorphic zircon populations, part of the crystals have Ti concentrations translating into apparent Ti-in-zircon temperatures above the thermal peak of metamorphism, which may indicate a lack of re-equilibration of an inherited Ti content (Appendix S10). The question of whether the high proportion of discordant U–Pb data (Appendix S8) results from incomplete resetting of inherited U–Pb isotopic systematics during metamorphic zircon growth or records later disturbances during the tectonic assembly of the SGM and the post-orogenic magmatism is not reliably resolvable, but the former likely played a major role taking into account indications of trace element disequilibrium. The high-*P* amphibolite facies metamorphism in the MSU was roughly coeval with the eclogite facies metamorphism in the Marianské Lázně Complex, where metamorphic zircon in eclogite ranging in size to more than 150 μm crystallized along with hornblende during decompression-related hydration (Timmermann et al., 2004, their sample HT-99-11). In the eastern Erzgebirge to the southeast of our study area, metamorphic zircon of Variscan age is associated with amphibole-plagioclase symplectite replacing omphacite in strongly retrogressed eclogite. Tichomirowa and Köhler (2013) have interpreted the euhedral to anhedral shaped zircon of more than 100 μm in size as relating to retrograde zircon dissolution–reprecipitation during fluid infiltration and concomitant release of Zr from decomposing omphacite. Weakly retrogressed eclogite from the same area in which zircon dissolution–reprecipitation did not occur preserves protolith zircon of Early Cambrian age.

An Ar–Ar age of 341 ± 2 Ma for the coarse amphibole grain-size fraction (Amp1) of metagabbro Böh2 defines a minimum age limit for cooling from the high-*P* phase of metamorphism in the MSU, considering that this coarse fraction may have undergone partial Ar loss during a subsequent phase of metamorphism related to the juxtaposition of the MSU with the granulite body, when all Ar was released from fine amphibole (Amp2). The onset of argon retention in fine amphibole from garnet amphibolite Krb1 at 334 ± 1 Ma in comparison to that in coarse amphibole from metagabbro Böh2 suggests that volume diffusion was crucial in controlling the Ar release, in particular as the fine amphibole from sample Krb1 underwent no post-peak recrystallization. However, chlorite overgrown on fractured garnet suggests that late deformation and fluid flow facilitated the isotope exchange in amphibole (Figure 3f). The Ar–Ar amphibole data thus provide evidence that cooling of the MSU following high-*P* metamorphism took place not later than 341 ± 2 Ma. The tectonic assembly of the SGM in the upper crust involved reheating of the MSU, which resulted in total Ar loss from fine amphibole until renewed cooling at 334 ± 1 Ma. Considering the preservation of old Ar–Ar amphibole ages, this thermal pulse was rather similar to that in the Schist Cover with which the MSU may have merged prior to its juxtaposition against the exhuming deeper structural units (Figure 18).

Late Carboniferous to early Permian magmatism in central Europe that spread over transtensional fault zones and related pull-apart basins like those in the Erzgebirge and the Erzgebirge Basin south of the SGM (Mattern, 2001; Romer, Thomas, Stein, & Rhede, 2007; Schneider & Romer, 2010) had a thermal impact on Variscan basement rocks, as shown by Ar–Ar amphibole ages for MSU metabasites in the range 317–307 Ma. Pervasive reheating above the closure temperature of the K–Ar system in hornblende at 530 ± 30°C (Harrison, 1981) is unlikely at this time because the ages postdate metamorphism. However, if fluid-induced grain boundary diffusion enhances element mobility, chronometric minerals may lose daughter isotopes at temperatures much lower than those defined by volume diffusion on which the concept of closure temperatures is based (Villa, 1998). We interpret the apparent Ar–Ar amphibole ages of 317–307 Ma as resulting from partial Ar loss during intense early Permian volcanism in proximity to the SGM, rather than from total Ar loss during distant or minor proximal, contemporaneous magmatism. An Ar–Ar amphibole plateau age of 270 ± 8 Ma for amphibolite Gröb1 of the MSU is below the lower error limit for a SHRIMP U-Pb zircon age of 289 ± 4 Ma interpreted as dating the terminal episode of the early Permian magmatism in the vicinity of the SGM (Hoffmann et al., 2013). However, the time when magmatism ceased remains obscure

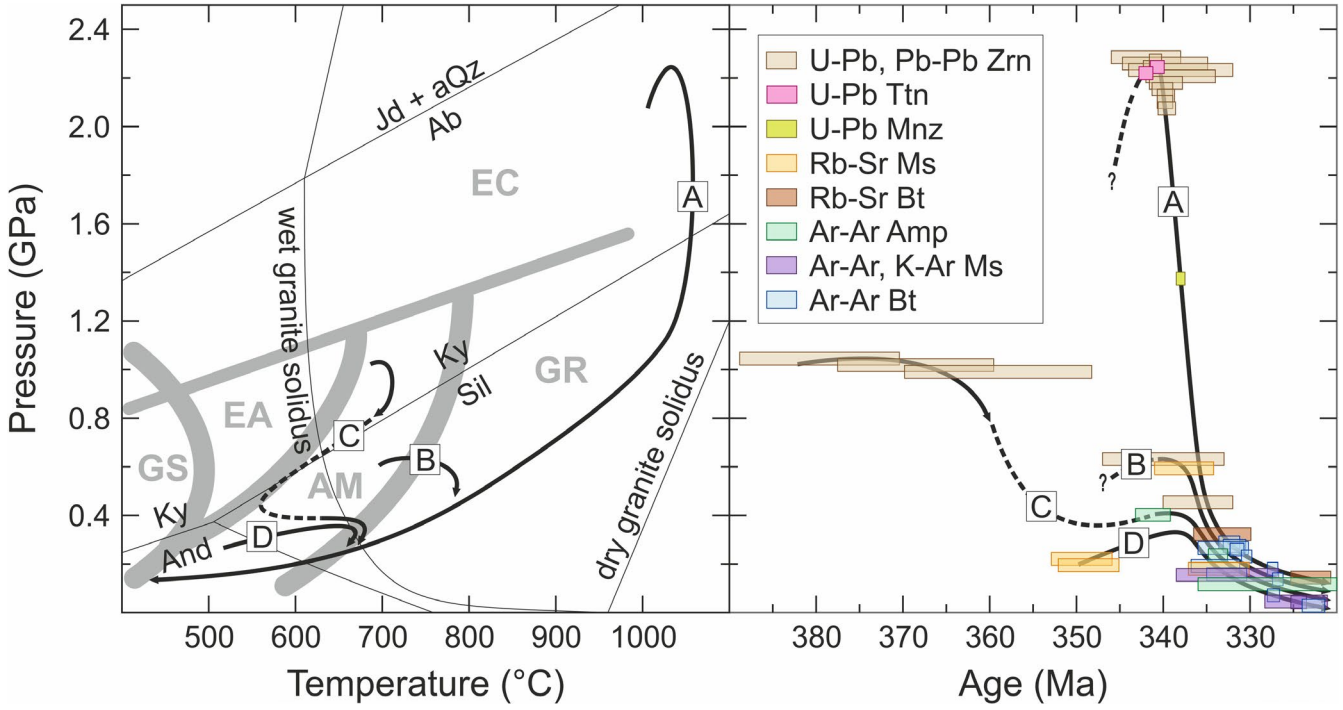

FIGURE 18 Metamorphic pressure–temperature and pressure–time paths for the granulite body (A), the Cordierite-Gneiss Unit (B), and the Schist Cover (D) in the Saxon Granulite Massif modified after Rötzler and Romer (2010) using the results of this study, in particular about the Metagabbro/Serpentinite Unit (C). Metamorphic facies boundaries (thick grey lines) for the greenschist (GS), epidote–amphibolite (EA), amphibolite (AM), granulite (GR) and eclogite (EC) facies are from Spear (1993); wet and dry haplogranite solidus curves after Johannes and Holtz (1996). Mineral abbreviations are from Whitney and Evans (2010)

because erosional unconformities truncating the North Saxon Volcanic Complex have removed the youngest volcanic record. A U–Pb zircon upper intercept age of 274 ± 5 Ma for rhyolite of the Thuringian Forest Basin (Lützner, Littmann, Mädler, Romer, & Schneider, 2003) suggests regional magmatic activity until the end of the early Permian.

Ar–Ar biotite ages in the range 332–327 Ma obtained in this study for Saxon granulites (Table 2) show a weak trend towards younger ages in the core than the margin of the granulite body that likely indicates cooling during or after formation of retrograde biotite. Rötzler et al. (2004) inferred from a correlation of U–Pb titanite and Rb–Sr biotite ages with petrologic data that exhumation and cooling of the granulite body occurred at mean rates of ~10 mm/year and ~50°C/Ma. Retrograde oxygen isotope fractionation suggests an average rate of 50–80°C/Ma for cooling of the granulite body to medium temperatures (Hagen et al., 2008). Assuming that biotite began to retain Ar quantitatively *c*. 332 Ma at *P–T* conditions of 0.2 GPa and 350°C, and relating this point on the retrograde path to the peak metamorphic stage at *c*. 341 Ma at *P–T* conditions of 2.2 GPa and 1,050°C yields average exhumation and cooling rates of ~8 mm/year and ~80°C/Ma. Evidence of peak-metamorphic titanite growth (Rötzler et al., 2004) justifies linking consistent U–Pb titanite and zircon ages to the equilibrium *P–T* conditions for the peak mineral assemblages, provided that the ages date mineral growth. The preservation of inherited and protolith zircon (Sagawe et al., 2016) indicates that the U–Pb zircon system remained closed at the peak of metamorphism. Romer and Rötzler (2001) tried to model the variation in exhumation and cooling rate by linking zircon, monazite and biotite ages to the *P–T* path for the granulite body. They used an Rb-Sr biotite age of 323 ± 2 Ma interpreted as dating cooling of the core of the granulite body below the Rb-Sr biotite closure temperature. The late exhumation and cooling rates thus calculated are too low because this age is clearly younger than the Ar–Ar biotite ages of *c*. 332 Ma obtained herein for nearby localities of the same rock type. The main obstacle to this modelling approach is the uncertainty on the actual monazite closure temperature. A monazite-bearing granulite with minor hydrous overgrowths led Romer and Rötzler (2001) to consider higher temperatures of 750–950°C than commonly assumed for the onset of Pb retention in monazite. Recalculated exhumation and cooling rates based on the above-mentioned *P–T–t* data for the peak of metamorphism and the beginning of Ar retention in biotite, and on a point along the *P–T* path at 0.6 GPa and 850°C related to the onset of Pb retention in monazite *c*. 338 Ma, suggest a drop in exhumation rate from ~20 mm/year to ~2.5 mm/year and a slight rise in cooling rate from ~70 to ~80°C/Ma. The exhumation rate decreases strongly,

independent of the chosen monazite closure temperature. By contrast, the trend to higher cooling rates reverses at monazite closure temperatures below ~820°C. Late cooling after the assembly of the SGM occurred at a high rate, as shown by the short time lag between the closure to Ar diffusion in amphibole of the MSU and biotite of the granulite body at *c*. 334 and *c*. 332 Ma, respectively. The Ar closure temperatures of 530°C for hornblende and 350°C for biotite (Harrison, 1981; Harrison, Duncan, & McDougall, 1985) when related to this time lag translate into a cooling rate of 90°C/Ma, suggesting that monazite closed to Pb diffusion above ~820°C.

Our Ar–Ar data show a trend to younger mica ages upwards in the structural section on top of the granulite body (Figure 15) that contrasts with some almost invariable Ar–Ar and K–Ar mica ages *c*. 333 Ma determined by Werner and Reich (1997) both near and far above the granulite contact (Figure 2). This divergence is unrelated to grain size differences because the 200–315 μm fractions used by Werner and Reich (1997; see Werner, 1998) are in the same range as our fractions (Table 2). Ductile deformation and cooling from metamorphism ceased during the granite intrusions at 335–333 Ma (Figure 2) and thus do not account for subsequent partial or total Ar loss from micas, which rather results from interaction with circulating fluid during post-orogenic, in particular early Permian, magmatism. K–Ar mica dating of phyllite from the northwestern Schist Cover (Marheine, 1997) using the grain-size fractions <0.2 μm and 0.2–2 μm has yielded ages of 294–297 Ma and 316–321 Ma, respectively (Figure 2). The younger ages suggest total Ar loss during formation of the North Saxon Volcanic Complex in the period 290–300 Ma (Hoffmann et al., 2013).

Rb-Sr muscovite and biotite dating of metasediments exposed within 750 m of the granulite contact along a traverse across the lower Schist Cover of the SGM has yielded older muscovite than associated biotite ages (Rötzler & Romer, 2010). Muscovite ages of *c*. 349 Ma obtained from the two samples highest in section (G97-7 and G97-8 in Figure 2) date an early phase of regional metamorphism prior to the emplacement of the granulite body. The deepest sample in section (G97-5 in Figure 2) taken from the sillimanite-K-feldspar zone of the Schist Cover contains retrograde muscovite, grown at early post-peak conditions, with an Rb–Sr age of 333.6 ± 3.5 Ma. Deformation and fluid flow along brittle normal and transverse faults have reset the Rb-Sr mica systems in the middle of the traverse, where ages below 290 Ma suggest a relation to the post-orogenic magmatism of the North Saxon Volcanic Complex. The Ar–Ar muscovite and biotite ages obtained in this study for sample G97-7 (Figure 15) are in between the respective Rb-Sr muscovite and biotite ages, with an inverse age relationship of muscovite to biotite suggesting that biotite closed to Ar diffusion earlier than muscovite. The Ar–Ar mica ages do not record earlier regional metamorphism, certainly because the thermal pulses during emplacement of the granulite body and post-orogenic magmatism were sufficiently strong to mobilize Ar while the more robust Rb-Sr muscovite system remained closed.

The Moldanubian granulites exposed 200–300 km southeast of the SGM are in many aspects similar to the Saxon granulites. Their metamorphism culminated at *c*. 340 Ma (Schulmann et al., 2005; Teipel, Finger, & Rohrmüller, 2012) shortly after calc-alkaline magmatism had begun in the subducting continental crust *c*. 345 Ma (Lexa et al., 2011). Peak metamorphism at *P–T* conditions in the range 1.8–2.0 GPa and 800–1,000°C (Lexa et al., 2011; O'Brien, 2008) preceded near-isothermal exhumation to mid-crustal levels associated with subvertical fabric development. Low-scale melting of exhuming calc-alkaline granulite produced hyperpotassic granulite at ultrahigh-*T* conditions at *c*. 337 Ma (Janoušek, Krenn, Finger, Míková, & Frýda, 2007; Sláma et al., 2008). Schulmann et al. (2005) reported mean Pb-Pb zircon ages of 341.6 ± 6 Ma and 339.1 ± 1.1 Ma for melt patches in amphibolite boudins enclosed in retrogressed migmatitic felsic granulite. They inferred from the overlap between the ages for high-*P* metamorphism and medium-*P* migmatization that decompression from 1.8–2.0 GPa to 0.7–0.9 GPa occurred within the lower error range of 6 Ma for the least precise melt patch age, which translates into an average rate of ~7 mm/year for exhumation from the bottom of the crustal root to mid-crustal depths. Lexa et al. (2011) interpreted the more precise melt patch age of *c*. 339 Ma as dating the change from vertical extrusion to horizontal spreading of the granulite bodies, as defined by subhorizontal fabric development. The tecto-no-metamorphic evolution of the Saxon and Moldanubian granulites provides an important clue to the plate tectonic scenario because models relating these rocks to a single subduction–collision system (Faryad, Jedlicka, & Collett, 2013; Schulmann et al., 2014) have to reconcile similar exhumation periods and mechanisms with different tectonic transport distances resulting from the far away localities.

10.3 | Plate tectonic models

The two-plate model of Kroner and Romer (2013) assuming initiation of intra-Gondwana subduction after Gondwana had docked with Laurussia faces the following obstacles: (a) Palaeomagnetic data show that not just two major continental plates but also microplates located in between and drifting independently of one another from high to low southern latitudes collided with Laurussia and Gondwana during the Variscan orogeny (Tait, 1999). Major plate rotation as a peculiarity of the Teplá-Barrandian Unit is undetectable in other Variscan units, thus supporting the existence of microplates with individual drift histories (Schätz, 2004). Regional age variation among the oceanic fragments incorporated into the

Variscan belt suggests different continental break-up events along the northern Gondwana margin (Kryza & Pin, 2010). (b) After the Rheic Ocean as the supposedly only ocean basin separating Laurussia from Gondwana had closed, the only plate boundary force capable of driving intra-Gondwana subduction of continental crust to mantle depths would have been ridge push from the Palaeotethys Ocean, which ceased in the early Carboniferous when the Palaeotethys margin with Gondwana changed from passive to active (Moix et al., 2013). (c) The introduction of suboceanic mantle rocks into continental crust of the Moldanubian Unit during early Carboniferous high-*P* metamorphism (Medaris, Wang, Jelínek, Mihaljevič, & Jakeš, 2005; Medaris, Wang, Mísar, & Jelínek, 1990; Svojtka et al., 2016) is in conflict with intracontinental subduction. Sm-Nd mineral isochron ages of 377–370 Ma, 339 ± 10 Ma, and 336 ± 7 Ma are inferred to date the initial contact of hot mantle and cooler crust, the final merger of mantle and crustal rocks, and cooling from metamorphism, respectively (Medaris et al., 2005; Medaris, Beard, & Jelínek, 2006). (d) Intracontinental subduction is also not in line with the late Devonian Variscan blueschist metamorphism (Faryad & Kachlík, 2013; Maluski & Patočka, 1997). (e) Cambro-Ordovician sequences overlying the Cadomian basement of the Teplá-Barrandian Unit do not conform to the assumption that a lack of early Palaeozoic crustal thinning made this unit an unsubductable block without Variscan overprint. The northwestern part of the unit actually underwent polymetamorphism in Ordovician rift and Devonian supra-subduction zone settings (Peřesty et al., 2017). The upper-plate position rules out that the unit could cause the supposed subduction zone jamming. (f) The time period of metamorphism of *c*. 50 Ma for Saxothuringian oceanic and continental crust rocks (Schulmann et al., 2014; this study) contradicts episodic activities of short-lived intracontinental subduction zones in the late Devonian and the early Viséan.

The similarities between the Saxon and Moldanubian granulites suggest a common evolution, ranging from protolith formation, through deep subduction, to fast exhumation. Schulmann et al. (2014) argued that the Saxon and Moldanubian granulites followed different material paths through the same subduction–collision system, associated with exhumation of the Saxon granulites back along the subduction interface, and of the Moldanubian granulites by vertical extrusion of crustal-scale diapirs in the hinterland. However, evidence of different exhumation mechanisms appears to be absent. Eclogites of the Moldanubian Unit exposed along the eastern flank of the Teplá-Barrandian Unit record peak *P–T* conditions of ~2.4 GPa and ~650°C, followed by amphibolite facies overprinting. For this low geothermal gradient metamorphism, Faryad et al. (2013) excluded the possibility that the eclogites are eastward-subducted Saxothuringian oceanic crust emplaced below a hot backarc region. The eclogites and associated serpentinites are instead supposed to be westward-subducted Moldanubian oceanic lithosphere subducted and exhumed back along the same interface (Faryad et al., 2013). This subduction system would be anti-parallel to that outlined by Schulmann et al. (2014) but would not involve lower crustal flow. However, the assumption that even Saxothuringian high-*P* rocks, including the Saxon granulites, were exhumed from this system and emplaced by long-distance thrusting in the upper crust cannot be reconciled with, for instance, the structural evolution and the diapir-like geometry of the Saxon granulites, which, according to geophysical data, extend downward to a minimum depth of 7 km (Krawczyk et al., 2000). The discrepancy seems to be resolvable by assuming bipolar subduction of Saxothuringian and Moldanubian crust below the Teplá-Barrandian microplate (Franke, 2000). The Saxon and Moldanubian granulites may thus originate from similar peri-Gondwanan crustal sources and may have undergone basically similar but not spatially identical tectono-metamorphic processes.

The Metagabbro/Serpentinite Unit of the SGM fits well with regional evidence for early Palaeozoic MORB-type magmatism, whereas its oceanic affinity is incompatible with syn-collisional or intraplate magmatism during the Variscan orogeny. Our interpretation of the early Cambrian zircon of the MSU as protolith zircon is thus most plausible. The MSU underwent peak metamorphism at distinctly lower *P–T* conditions and earlier time than the Saxon granulites (Figure 18), meaning that the primary formation of the MSU cannot have caused the granulite metamorphism. Schulmann et al. (2014) have proposed underthrusting beneath the hot upper crust of a former backarc region as a mechanism as to how ultra-high-*T* metamorphism can be generated in deeply subducted continental crust rocks.

11 | CONCLUSIONS

1. The Saxon granulites derive from crustal sources in the rifted northern Gondwana margin, where oceanic opening produced the protoliths of the Metagabbro/Serpentinite Unit now overlying the granulites. Metasediments from the Schist Cover higher up in the section have West African and peri-Gondwanan provenances.
2. Zircon compositional and thermometric evidence and regional correlation suggest that a U-Pb zircon age of *c*. 532 Ma obtained from metagabbro is the most likely age of the oceanic magmatism in the Metagabbro/Serpentinite Unit. Saturation models indicate that the Zr concentrations in the studied and other zircon-bearing MORB-type rocks of the Variscan belt are too low for zircon to crystallize from melt equivalent to the bulk rock. Intercumulus melt higher in Zr content, but lower in Zr solubility than melt equivalent to the bulk rock, or transient disequilibrium melt enriched in Zr at interfaces of rapidly growing

cumulus phases or at sites of rapidly dissolved inherited zircon are melt fractions that may precipitate zircon in otherwise Zr-undersaturated bulk melt compositions.

3. The stratigraphic age of metasediments in the upper part of the Schist Cover, dated palynologically as Neoproterozoic (Heuse et al., 1994, 2010), is not older than Middle/Upper Devonian boundary time, based on detrital zircon dating, and thus fits well into the right-way-up sequence of the Schist Cover.
4. Metamorphism in the Metagabbro/Serpentinite Unit was polyphase. The first phase, dated by U-Pb zircon as mid- to late-Devonian and hence older than the metamorphism in the adjacent continental crust units, followed a clockwise *P–T* path, with peak conditions slightly above 1.0 GPa and 700°C. Cooling from this early phase occurred at *c*. 341 Ma at the latest, based on Ar–Ar dating of coarse amphibole. The second phase reflects isobaric heating by the exhuming granulite body in the upper crust, associated with resetting of fine amphibole until renewed cooling *c*. 334 Ma.
5. A younging-inward progression in Ar–Ar biotite ages in the granulite body records cooling of the Saxon granulites during the period 332–327 Ma. Ar–Ar and K–Ar mica ages in the overlying units reveal that cooling of these units *c*. 333 Ma preceded partial resetting caused by early Permian geothermal activity. Ar–Ar amphibole ages suggest similar resetting, but one notably young age indicates resetting some time after the supposed end of volcanism.
6. Exhumation and cooling of the Saxon granulites from peak metamorphism to argon retention in biotite occurred at average rates of ~8 mm/year and ~80°C/Ma. An evaluation of the rates using monazite as a chronometer to distinguish early near-isothermal decompression from late decompressional cooling of the granulites shows that the exhumation rate decreased strongly from ~20 to ~2.5 mm/year while the cooling rate increased slightly from ~70 to ~80°C/Ma. The different closure temperatures to argon diffusion in hornblende and biotite when related to Ar–Ar ages for amphibole in the Metagabbro/Serpentinite Unit and for biotite in the granulite body translate into a cooling rate of 90°C/Ma after all units had assembled into the massif.
7. A two-plate model for the Variscan orogeny (Kroner & Romer, 2013) is in conflict with several lines of evidence, such as, for instance, the presence of microplates with distinct drift histories (Schätz, 2004; Tait, 1999), or of oceanic fragments that record different events of oceanic opening (Kryza & Pin, 2010) and cannot be related to intracontinental subduction zones (Medaris et al., 2005, 2006; Svojtka et al., 2016; this study). Tectonic models in which the exhumation of the Saxon and Modanubian granulites from a common, either east or west-directed, subduction system is attributed to different material paths (Schulmann et al., 2014), including intense upper crustal thrusting of the Saxon granulites (Faryad et al., 2013), do not agree with the similarity in fabric evolution and exhumation period between these rocks, and with the large depth extent of the Saxon granulites (Krawczyk et al., 2000). This discrepancy disappears if we consider bipolar subduction of Saxothuringian and Moldanubian crust below the Teplá-Barrandian microplate (Franke, 2000).

ACKNOWLEDGEMENTS

The Deutsche Forschungsgemeinschaft supported this work under grant OB 80/44-1. Other researchers, technicians and students helped accomplish the goals by providing samples, carrying out sample preparation, and assisting with the scanning electron microscopy, electron probe microanalysis and mass spectrometry, including Christine Fischer, Christina Günther, Jens Krüger, Alexander Schmidt, Masafumi Sudo, Martin Wieschalla (all of University of Potsdam), Oona Appelt, Juliane Herwig, Hartmut Liep, Rolf L. Romer and Ilona Schäpan (all of German Research Centre for Geosciences, GFZ). The GFZ co-financed the project by covering the cost of all activities undertaken there, in addition to part of the travelling expenses and student assistant wages. We thank Katy Evans for her editorial handling of the manuscript. Shah Wali Faryad and an anonymous reviewer thoroughly examined the manuscript and made valuable suggestions to improve it. Open access funding enabled and organized by Projekt DEAL.

ORCID

Jochen Rötzler https://orcid.org/0000-0003-2963-4675

REFERENCES

Bacon, C. R. (1989). Crystallization of accessory phases in magmas by local saturation adjacent to phenocrysts. *Geochimica et Cosmochimica Acta*, *53*, 1055–1066. https://doi.org/10.1016/0016-7037(89)90210-X

Bankwitz, P., Bankwitz, E., Kramer, W., & Pin, C. (1994). Early Paleozoic bimodal volcanism in the Vesser area, Thuringian Forest, eastern Germany. *Zentralblatt für Geologie und Paläontologie, Teil I*, *1992*, 1113–1132.

Bea, F., Montero, P., Molina, J. F., Scarrow, J. H., Cambeses, A., & Moreno, J. A. (2018). Lu-Hf ratios of crustal rocks and their bearing on zircon Hf isotope model ages: The effects of accessories. *Chemical Geology*, *484*, 179–190. https://doi.org/10.1016/j.chemgeo.2017.11.034

Behr, H.-J. (1961). Beiträge zur petrographischen und tektonischen Analyse des sächsischen Granulitgebirges. *Freiberger Forschungshefte, C*, *119*, 5–118.

Belousova, E. A., Griffin, W. L., O'Reilly, S. Y., & Fisher, N. I. (2002). Igneous zircon: Trace element composition as an indicator of source rock type. *Contributions to Mineralogy and Petrology*, *143*, 602–622. https://doi.org/10.1007/s00410-002-0364-7

Cambeses, A., Scarrow, J. H., Montero, P., Lázaro, C., & Bea, F. (2017). Palaeogeography and crustal evolution of the Ossa-Morena Zone,

southwest Iberia, and the North Gondwana margin during the Cambro-Ordovician: A review of isotopic evidence. *International Geology Review*, *59*, 94–130. https://doi.org/10.1080/00206814.2016.1219279

Clark, A. H., Scott, D. J., Sandeman, H. A., Bromley, A. V., & Farrar, E. (1998). Siegenian generation of the Lizard ophiolite: U-Pb zircon age data for plagiogranite, Porthkerris, Cornwall. *Journal of the Geological Society, London*, *155*, 595–598. https://doi.org/10.1144/gsjgs.155.4.0595

Cocks, L. R. M., & Fortey, R. A. (2009). Avalonia: a long-lived terrane in the Lower Palaeozoic? In: M. G. Bassett (Ed.), *Early Palaeozoic Peri-Gondwana Terranes: New Insights from Tectonics and Biogeography*. *Geological Society, London, Special Publications*, *325*, 141–155.

Cook, C. A., Holdsworth, R. E., & Styles, M. T. (2002). The emplacement of peridotites and associated oceanic rocks from the Lizard Complex, southwest England. *Geological Magazine*, *139*, 27–45. https://doi.org/10.1017/S0016756801005933

Cook, C. A., Holdsworth, R. E., Styles, M. T., & Pearce, J. A. (2000). Pre-emplacement structural history recorded by mantle peridotites: An example from the Lizard Complex, SW England. *Journal of the Geological Society, London*, *157*, 1049–1064. https://doi.org/10.1144/jgs.157.5.1049

de Capitani, C., & Petrakakis, K. (2010). The computation of equilibrium assemblage diagrams with Theriak/Domino software. *American Mineralogist*, *95*, 1006–1016. https://doi.org/10.2138/am.2010.3354

Díez Fernández, R., Pereira, M. F., & Foster, D. A. (2015). Peralkaline and alkaline magmatism of the Ossa-Morena zone (SW Iberia): Age, source, and implications for the Paleozoic evolution of Gondwanan lithosphere. *Lithosphere*, *7*, 73–90. https://doi.org/10.1130/L379.1

Dubińska, E., Bylina, P., Kozłowski, A., Dörr, W., Nejbert, K., Schastok, J., & Kulicki, C. (2004). U-Pb dating of serpentinization: Hydrothermal zircon from a metasomatic rodingite shell (Sudetic ophiolite, SW Poland). *Chemical Geology*, *203*, 183–203. https://doi.org/10.1016/j.chemgeo.2003.10.005

Faryad, S. W., Jedlicka, R., & Collett, S. (2013). Eclogite facies rocks of the Monotonous unit, clue to Variscan suture in the Moldanubian Zone (Bohemian Massif). *Lithos*, *179*, 353–363. https://doi.org/10.1016/j.lithos.2013.07.015

Faryad, S. W., & Kachlík, V. (2013). New evidence of blueschist facies rocks and their geotectonic implication for Variscan suture(s) in the Bohemian Massif. *Journal of Metamorphic Geology*, *31*, 63–82. https://doi.org/10.1111/jmg.12009

Ferry, J. M., & Watson, E. B. (2007). New thermodynamic models and revised calibrations for the Ti-in-zircon and Zr-in-rutile thermometers. *Contributions to Mineralogy and Petrology*, *154*, 429–437. https://doi.org/10.1007/s00410-007-0201-0

Fleck, R. J., Sutter, J. F., & Elliot, D. H. (1977). Interpretation of discordant $^{40}Ar/^{39}Ar$ age-spectra of Mesozoic tholeiites from Antarctica. *Geochimica et Cosmochimica Acta*, *41*, 15–32. https://doi.org/10.1016/0016-7037(77)90184-3

Franke, W. (2000). The mid-European segment of the Variscides: tectonostratigraphic units, terrane boundaries and plate tectonic evolution. In: W. Franke, V. Haak, O. Oncken, & D. Tanner (Eds.), *Orogenic Processes: Quantification and Modelling in the Variscan Belt*. *Geological Society, London, Special Publications*, *179*, 35–61.

Gebauer, D., & Grünenfelder, M. (1979). U-Pb zircon and Rb-Sr mineral dating of eclogites and their country rocks. Example: Münchberg gneiss massif, Northeast Bavaria. *Earth and Planetary Science Letters*, *42*, 35–44. https://doi.org/10.1016/0012-821X(79)90188-2

Goodge, J. W., Fanning, C. M., & Bennett, V. C. (2001). U-Pb evidence of ~1.7 Ga crustal tectonism during the Nimrod Orogeny in the Transantarctic Mountains, Antarctica: Implications for Proterozoic plate reconstructions. *Precambrian Research*, *112*, 261–288. https://doi.org/10.1016/S0301-9268(01)00193-0

Gottesmann, B., Tischendorf, G., & Wand, U. (1994). Die granitoiden Gesteine des Sächsischen Granulitmassivs – Petrographie, Geochemie und Altersstellung. *Hallesches Jahrbuch für Geowissenschaften*, *16*, 23–55.

Grad, M., Guterch, A., Mazur, S., Keller, G. R., Špičák, A., Hrubcová, P., & Geissler, W. H. (2008). Lithospheric structure of the Bohemian Massif and adjacent Variscan belt in central Europe based on profile S01 from the SUDETES 2003 experiment. *Journal of Geophysical Research*, *113*, B10304. https://doi.org/10.1029/2007JB005497

Grew, E. S. (1986). Petrogenesis of kornerupine at Waldheim (Sachsen), German Democratic Republic. *Zeitschrift für Geologische Wissenschaften*, *14*, 525–558.

Hagen, B., Hoernes, S., & Rötzler, J. (2008). Geothermometry of the ultrahigh-temperature Saxon granulites revisited. Part II: Thermal peak conditions and cooling rates inferred from oxygen-isotope fractionations. *European Journal of Mineralogy*, *20*, 1117–1133. https://doi.org/10.1127/0935-1221/2008/0020-1858

Harrison, T. M. (1981). Diffusion of ^{40}Ar in hornblende. *Contributions to Mineralogy and Petrology*, *78*, 324–331.

Harrison, T. M., Duncan, I., & McDougall, I. (1985). Diffusion of ^{40}Ar in biotite: Temperature, pressure and compositional effects. *Geochimica et Cosmochimica Acta*, *49*, 2461–2468. https://doi.org/10.1016/0016-7037(85)90246-7

Hawthorne, F. C., Oberti, R., Harlow, G. E., Maresch, W. V., Martin, R. F., Schumacher, J. C., & Welch, M. D. (2012). IMA Report: Nomenclature of the amphibole supergroup. *American Mineralogist*, *97*, 2031–2048. https://doi.org/10.2138/am.2012.4276

Henderson, B. J., Collins, W. J., Murphy, J. B., Gutierrez-Alonso, G., & Handa, M. (2016). Gondwanan basement terranes of the Variscan-Appalachian orogen: Baltican, Saharan and West African hafnium isotopic fingerprints in Avalonia, Iberia and the Armorican Terranes. *Tectonophysics*, *681*, 278–304. https://doi.org/10.1016/j.tecto.2015.11.020

Heuse, T., Blumenstengel, H., Elicki, O., Geyer, G., Hansch, W., Maletz, J., … Weyer, D. (2010). Biostratigraphy – The faunal province of the southern margin of the Rheic Ocean. In U. Linnemann, & R. L. Romer (Eds.), *Pre-Mesozoic Geology of Saxo-Thuringia: From the Cadomian Active Margin to the Variscan Orogen* (pp. 99–170). Stuttgart, Germany: Schweizerbart.

Heuse, T., Kurze, M., & Reitz, E. (1994). Paläontologischer Nachweis von Oberproterozoikum (Vendium) in der Zone Münchberg-Frankenberg. *Neues Jahrbuch für Geologie und Paläontologie, Monatshefte*, *1994*, 95–107.

Hoffmann, U., Breitkreuz, C., Breiter, K., Sergeev, S., Stanek, K., & Tichomirowa, M. (2013). Carboniferous-Permian volcanic evolution in Central Europe – U/Pb ages of volcanic rocks in Saxony (Germany) and northern Bohemia (Czech Republic). *International Journal of Earth Sciences*, *102*, 73–99. https://doi.org/10.1007/s00531-012-0791-2

Höhn, S., Koglin, N., Klopf, L., Schüssler, U., Tragelehn, H., Frimmel, H. E., … Brätz, H. (2018). Geochronology, stratigraphy and geochemistry of Cambro-Ordovician, Silurian and Devonian volcanic rocks of the Saxothuringian Zone in NE Bavaria (Germany) – New

constraints for Gondwana break up and ocean-island magmatism. *International Journal of Earth Sciences*, *107*, 359–377. https://doi.org/10.1007/s00531-017-1497-2

Holland, T. J. B., & Powell, R. (1998). An internally-consistent thermodynamic data set for phases of petrological interest. *Journal of Metamorphic Geology*, *16*, 309–343. https://doi.org/10.1111/j.1525-1314.1998.00140.x

Jaeckel, P., Anthes, G., Molzahn, M., Oncken, O., & Reischmann, T. (1999). Pb isotopic systematics of the Central Variscan belt. *Terra Nostra*, *99*(1), 111–112.

Janoušek, V. (2006). Saturnin, R language script for application of accessory-mineral saturation models in igneous geochemistry. *Geologica Carpathica*, *57*, 131–142.

Janoušek, V., Krenn, E., Finger, F., Míková, J., & Frýda, J. (2007). Hyperpotassic granulites from Blanský les (Moldanubian Zone, Bohemian Massif) revisited. *Journal of Geosciences*, *52*, 73–112.

Johannes, W., & Holtz, F. (1996). *Petrogenesis and experimental petrology of granitic rocks*. Berlin, Germany: Springer-Verlag. 335 pp.

Kemnitz, H., Romer, R. L., & Oncken, O. (2002). Gondawana break-up and the northern margin of the Saxothuringian belt (Variscides of Central Europe). *International Journal of Earth Sciences*, *91*, 246–259.

Kossow, D. (2002). Die kinematische Entwicklung des invertierten, intrakontinentalen Nordostdeutschen Beckens. Potsdam: Deutsches GeoForschungsZentrum GFZ, Scientific Technical Report, 02/04, 101 pp.

Krawczyk, C. M., Stein, E., Choi, S., Oettinger, G., Schuster, K., Götze, H.-J., Schulze, A. (2000). Geophysical constraints on exhumation mechanisms of high-pressure rocks: the Saxo-Thuringian case between the Franconian Line and Elbe Zone. In: W. Franke, V. Haak, O. Oncken, & D. Tanner (Eds.), *Orogenic Processes: Quantification and Modelling in the Variscan Belt*. *Geological Society, London, Special Publications*, *179*, 303–322.

Kreuzer, H., Seidel, E., Schüssler, U., Okrusch, M., Lenz, K.-L., & Raschka, H. (1989). K-Ar geochronology of different tectonic units at the northwestern margin of the Bohemian Massif. *Tectonophysics*, *157*, 149–178. https://doi.org/10.1016/0040-1951(89)90348-X

Kröner, A., Jaeckel, P., Reischmann, T., & Kroner, U. (1998). Further evidence for an early Carboniferous (~340 Ma) age of high-grade metamorphism in the Saxonian granulite complex. *International Journal of Earth Sciences*, *86*, 751–766. https://doi.org/10.1007/PL00009939

Kroner, U. (1995). Postkollisionale Extension am Nordrand des Böhmischen Massivs: Die Exhumierung des Sächsischen Granulitgebirges. *Freiberger Forschungshefte, C*, *457*, 1–114.

Kroner, U., Hahn, T., Romer, R. L., & Linnemann, U. (2007). The Variscan orogeny in the Saxo-Thuringian zone—Heterogenous overprint of Cadomian/Paleozoic Peri-Gondwana crust. *Geological Society of America Special Paper*, *423*, 153–172.

Kroner, U., & Romer, R. L. (2013). Two plates – Many subduction zones: The Variscan orogeny reconsidered. *Gondwana Research*, *24*, 298–329. https://doi.org/10.1016/j.gr.2013.03.001

Kryza, R., & Fanning, C. M. (2007). Devonian deep-crustal metamorphism and exhumation in the Variscan Orogen: Evidence from SHRIMP zircon ages from the HT-HP granulites and migmatites of the Góry Sowie (Polish Sudetes). *Geodinamica Acta*, *20*(3), 159–175. https://doi.org/10.3166/ga.20.159-175

Kryza, R., & Pin, C. (2010). The Central-Sudetic ophiolites (SW Poland): Petrogenetic issues, geochronology and palaeotectonic implications. *Gondwana Research*, *17*, 292–305. https://doi.org/10.1016/j.gr.2009.11.001

Kusbach, V., Janoušek, V., Hasalová, P., Schulmann, K., Fanning, C. M., Erban, V., & Ulrich, S. (2015). Importance of crustal relamination in origin of the orogenic mantle peridotite-high-pressure granulite association: Example from the Náměšť Granulite Massif (Bohemian Massif, Czech Republic). *Journal of the Geological Society*, *172*, 479–490. https://doi.org/10.1144/jgs2014-070

Lexa, O., Schulmann, K., Janoušek, V., Štípská, P., Guy, A., & Racek, M. (2011). Heat sources and trigger mechanisms of exhumation of HP granulites in Variscan orogenic root. *Journal of Metamorphic Geology*, *29*, 79–102. https://doi.org/10.1111/j.1525-1314.2010.00906.x

Linnemann, U., Gerdes, A., Drost, K., & Buschmann, B. (2007). The continuum between Cadomian orogenesis and opening of the Rheic Ocean: Constraints from LA-ICP-MS U-Pb zircon dating and analysis of plate-tectonic setting (Saxo-Thuringian zone, northeastern Bohemian Massif, Germany). *Geological Society of America Special Paper*, *423*, 61–96.

Locock, A. J. (2014). An Excel spreadsheet to classify chemical analyses of amphiboles following the IMA 2012 recommendations. *Computers & Geosciences*, *62*, 1–11. https://doi.org/10.1016/j.cageo.2013.09.011

Lorenz, W., & Nitzsche, H.-M. (2000). Stratigraphische Konzepte, Metamorphose und Kohlenstoffisotope im Rahmen und im Kern des sächsischen Granulitgebirges. *Zeitschrift für Geologische Wissenschaften*, *28*, 321–360.

Lünser, C. (1994). Ophiolitic gabbros and diabases of the Saxon Granulite Massif. *Zentralblatt für Geologie und Paläontologie, Teil I*, *1992*(9/10), 1071–1085.

Lützner, H., Littmann, S., Mädler, J., Romer, R. L., & Schneider, J. W. (2003). Radiometric and biostratigraphic data of the Permocarboniferous reference section Thüringer Wald. 15th International Congress on Carboniferous and Permian Stratigraphy. Utrecht, the Netherlands, 10–16 August 2003. Proceedings, pp. 161–174.

Maluski, H., & Patočka, F. (1997). Geochemistry and ^{40}Ar-^{39}Ar geochronology of the mafic metavolcanic rocks from the Rýchory Mountains complex (west Sudetes, Bohemian Massif): Palaeotectonic significance. *Geological Magazine*, *134*, 703–716.

Marheine, D. (1997). Zeitmarken im variszischen Kollisionsbereich des Rhenoherzynikums-Saxothuringikums zwischen Harz und Sächsischem Granulitmassiv. *Göttinger Arbeiten zur Geologie und Paläontologie*, *75*, 97.

Mattern, F. (2001). Permo-Silesian movements between Baltica and Western Europe: Tectonics and 'basin families'. *Terra Nova*, *13*, 368–375. https://doi.org/10.1046/j.1365-3121.2001.00368.x

McDonough, W. F., & Sun, S.-S. (1995). The composition of the Earth. *Chemical Geology*, *120*, 223–253. https://doi.org/10.1016/0009-2541(94)00140-4

Medaris, G. Jr, Wang, H., Jelínek, E., Mihaljevič, M., & Jakeš, P. (2005). Characteristics and origins of diverse Variscan peridotites in the Gföhl Nappe, Bohemian Massif, Czech Republic. *Lithos*, *82*, 1–23. https://doi.org/10.1016/j.lithos.2004.12.004

Medaris, L. G. Jr, Beard, B. L., & Jelínek, E. (2006). Mantle-derived, UHP garnet pyroxenite and eclogite in the Moldanubian Gföhl Nappe, Bohemian Massif: A geochemical review, new P-T determinations, and tectonic interpretation. *International Geology Review*, *48*, 765–777. https://doi.org/10.2747/0020-6814.48.9.765

Medaris, L. G., Wang, H. F., Mísar, Z., & Jelínek, E. (1990). Thermobarometry, diffusion modeling and cooling rates of crustal garnet peridotites: Two examples from the Moldanubian zone of the Bohemian Massif. *Lithos*, *25*, 189–202.

Moix, P., Vachard, D., Allibon, J., Martini, R., Wernli, R., Kozur, H. W., & Stampfli, G. M. (2013). Palaeotethyan, Neotethyan and Huğlu-Pindos Series in the Lycian Nappes (SW Turkey): Geodynamical implication. In: L. H. Tanner, J. A. Spielmann, & S. G. Lucas (Eds.), *The Triassic system: New developments in stratigraphy and paleontology*. *New Mexico Museum of Natural History and Science Bulletin*, *61*, 401–444.

Muszer, J., & Haydukiewicz, J. (2011). The quarry in Dzikowiec as a geotouristic site and its importance for studies on the Upper Paleozoic in the Sudetes. In T. Słomka (Ed.), *Geotourism – A variety of aspects* (pp. 243–257). Kraków, Part III, Poland: AGH University of Science and Technology.

Nasdala, L., Pidgeon, R. T., Wolf, D., & Irmer, G. (1998). Metamictization and U-Pb isotopic discordance in single zircons: A combined Raman microprobe and SHRIMP ion probe study. *Mineralogy and Petrology*, *62*, 1–27. https://doi.org/10.1007/BF01173760

Nutman, A. P., Green, D. H., Cook, C. A., Styles, M. T., & Holdsworth, R. E. (2001). SHRIMP U-Pb zircon dating of the exhumation of the Lizard peridotite and its emplacement over crustal rocks: Constraints for tectonic models. *Journal of the Geological Society, London*, *158*, 809–820. https://doi.org/10.1144/jgs.158.5.809

O'Brien, P. J. (2008). Challenges in high-pressure granulite metamorphism in the era of pseudosections: Reaction textures, compositional zoning and tectonic interpretation with examples from the Bohemian Massif. *Journal of Metamorphic Geology*, *26*, 235–251. https://doi.org/10.1111/j.1525-1314.2007.00758.x

Oliver, G. J. H., Corfu, F., & Krogh, T. E. (1993). U-Pb ages from SW Poland: Evidence for a Caledonian suture zone between Baltica and Gondwana. *Journal of the Geological Society, London*, *150*, 355–369. https://doi.org/10.1144/gsjgs.150.2.0355

Pearce, J. A. (1976). Statistical analysis of major element patterns in basalt. *Journal of Petrology*, *17*, 15–43.

Peřestý, V., Lexa, O., Holder, R., Jeřábek, P., Racek, M., Štípská, P., … Hacker, B. (2017). Metamorphic inheritance of Rheic passive margin evolution and its early-Variscan overprint in the Teplá-Barrandian Unit, Bohemian Massif. *Journal of Metamorphic Geology*, *35*, 327–355. https://doi.org/10.1111/jmg.12234

Reinhardt, J., & Vavra, G. (1997). Petrological and geochronological constraints on the tectono-metamorphic history of the Saxonian Granulite Massif. *Terra Nostra*, *5*(97), 137–139.

Rioux, M., Jöns, N., Bowring, S., Lissenberg, C. J., Bach, W., Kylander-Clark, A., … Dudás, F. (2015). U-Pb dating of interspersed gabbroic magmatism and hydrothermal metamorphism during lower crustal accretion, Vema lithospheric section, Mid-Atlantic Ridge. *Jornal of Geophysical Research: Solid Earth*, *120*, 2093–2118. https://doi.org/10.1002/2014JB011668

Romer, R. L., & Hahne, K. (2010). Life of the Rheic Ocean: Scrolling through the shale record. *Gondwana Research*, *17*, 236–253. https://doi.org/10.1016/j.gr.2009.09.004

Romer, R. L., & Rötzler, J. (2001). P-T-t evolution of ultrahigh-temperature granulites from the Saxon Granulite Massif, Germany. Part II: U-Pb dating of trace and major phases. *Journal of Petrology*, *42*, 2015–2032.

Romer, R. L., Thomas, R., Stein, H. J., & Rhede, D. (2007). Dating multiply overprinted Sn-mineralized granites – Examples from the Erzgebirge, Germany. *Mineralium Deposita*, *42*, 337–359. https://doi.org/10.1007/s00126-006-0114-2

Rötzler, J., Carswell, D. A., Gerstenberger, H., & Haase, G. (1999). Transitional blueschist-epidote amphibolite facies metamorphism in the Frankenberg massif, Germany, and geotectonic implications. *Journal of Metamorphic Geology*, *17*, 109–125. https://doi.org/10.1046/j.1525-1314.1999.00183.x

Rötzler, J., Hagen, B., & Hoernes, S. (2008). Geothermometry of the ultrahigh-temperature Saxon granulites revisited. Part I: New evidence from key mineral assemblages and reaction textures. *European Journal of Mineralogy*, *20*, 1097–1115. https://doi.org/10.1127/0935-1221/2008/0020-1857

Rötzler, J., & Romer, R. L. (2001). P-T-t evolution of ultrahigh-temperature granulites from the Saxon Granulite Massif, Germany. Part I: Petrology. *Journal of Petrology*, *42*, 1995–2013. https://doi.org/10.1093/petrology/42.11.1995

Rötzler, J., & Romer, R. L. (2010). The Saxon Granulite Massif: A key area for the geodynamic evolution of Variscan central Europe. In U. Linnemann & R. L. Romer (Eds.), *Pre-Mesozoic Geology of Saxo-Thuringia: From the Cadomian Active Margin to the Variscan Orogen* (pp. 233–252). Stuttgart, Germany: Schweizerbart.

Rötzler, J., Romer, R. L., Budzinski, H., & Oberhänsli, R. (2004). Ultrahigh-temperature high-pressure granulites from Tirschheim, Saxon Granulite Massif, Germany: P-T-t path and geotectonic implications. *European Journal of Mineralogy*, *16*, 917–937. https://doi.org/10.1127/0935-1221/2004/0016-0917

Sagawe, A., Gärtner, A., Hofmann, M., & Linnemann, U. (2013). U-Pb ages and morphology of zircons from different granites within the Saxonian Granulite Massif. *Geologica Saxonica*, *59*, 205–224.

Sagawe, A., Gärtner, A., Linnemann, U., Hofmann, M., & Gerdes, A. (2016). Exotic crustal components at the northern margin of the Bohemian Massif – Implications from U-Th-Pb and Hf isotopes of zircon from the Saxonian Granulite Massif. *Tectonophysics*, *681*, 234–249. https://doi.org/10.1016/j.tecto.2016.04.013

Schätz, M. R. (2004). Palaeozoic geography and palaeomagnetism of the Central European Variscan and Alpine fold belts. München: Ludwig-Maximilians-Universität München. Doctoral thesis. 122 pp.

Schneider, J. W., & Romer, R. L. (2010). The Late Variscan molasses (Late Carboniferous to Late Permian) of the Saxo-Thuringian Zone. In U. Linnemann & R. L. Romer (Eds.), *Pre-Mesozoic Geology of Saxo-Thuringia: From the Cadomian Active Margin to the Variscan Orogen* (pp. 323–346). Stuttgart, Germany: Schweizerbart.

Schulmann, K., Kröner, A., Wendt, I., Hegner, E., Konopásek, J., Lexa, O., & Štípská, P. (2005). Chronological constraints on the pre-orogenic history, burial and exhumation of deep-seated rocks along the eastern margin of the Variscan orogen, Bohemian Massif, Czech Republic. *American Journal of Science*, *305*, 407–448. https://doi.org/10.2475/ajs.305.5.407

Schulmann, K., Lexa, O., Janoušek, V., Lardeaux, J. M., & Edel, J. B. (2014). Anatomy of a diffuse cryptic suture zone: An example from the Bohemian Massif, European Variscides. *Geology*, *42*, 275–278. https://doi.org/10.1130/G35290.1

Schulmann, K., Lexa, O., Štípská, P., Racek, M., Tajčmanová, L., Konopásek, J., … Lehmann, J. (2008). Vertical extrusion and horizontal channel flow of orogenic lower crust: Key exhumation mechanisms in large hot orogens? *Journal of Metamorphic Geology*, *26*, 273–297. https://doi.org/10.1111/j.1525-1314.2007.00755.x

Shao, T., Xia, Y., Ding, X., Cai, Y., & Song, M. (2019). Zircon saturation in terrestrial basaltic melts and its geological implications. *Solid Earth Sciences*, *4*, 27–42. https://doi.org/10.1016/j.sesci.2018.08.001

Sláma, J., Košler, J., Condon, D. J., Crowley, J. L., Gerdes, A., Hanchar, J. M., … Whitehouse, M. J. (2008). Plešovice zircon – A new natural reference material for U-Pb and Hf isotopic microanalysis. *Chemical Geology*, *249*, 1–35. https://doi.org/10.1016/j.chemgeo.2007.11.005

Soejono, I., Janoušek, V., Žáčková, E., Sláma, J., Konopásek, J., Machek, M., & Hanžl, P. (2017). Long-lasting Cadomian magmatic activity along an active northern Gondwana margin: U-Pb zircon and Sr-Nd isotopic evidence from the Brunovistulian Domain, eastern Bohemian Massif. *International Journal of Earth Sciences*, *106*, 2109–2129. https://doi.org/10.1007/s00531-016-1416-y

Spear, F. S. (1993). *Metamorphic phase equilibria and pressure-temperature-time paths*. Washington, DC: Mineralogical Society of America, 799 pp.

Spencer, C. J., Kirkland, C. L., Prave, A. R., Strachan, R. A., & Pease, V. (2019). Crustal reworking and orogenic styles inferred from zircon Hf isotopes: Proterozoic examples from the North Atlantic region. *Geoscience Frontiers*, *10*, 417–424. https://doi.org/10.1016/j.gsf.2018.09.008

Stosch, H.-G., & Lugmair, G. W. (1990). Geochemistry and evolution of MORB-type eclogites from the Münchberg Massif, southern Germany. *Earth and Planetary Science Letters*, *99*, 230–249. https://doi.org/10.1016/0012-821X(90)90113-C

Svojtka, M., Ackerman, L., Medaris, L. G., Hegner, E., Valley, J. W., Hirajima, T., … Hrstka, T. (2016). Petrological, geochemical and Sr-Nd-O isotopic constraints on the origin of garnet and spinel pyroxenites from the Moldanubian Zone of the Bohemian Massif. *Journal of Petrology*, *57*, 897–920. https://doi.org/10.1093/petrology/egw025

Tait, J. (1999). New Early Devonian paleomagnetic data from NW France: Paleogeography and implications for the Armorican microplate hypothesis. *Journal of Geophysical Research*, *104*, 2831–2839. https://doi.org/10.1029/98JB02787

Teipel, U., Finger, F., & Rohrmüller, J. (2012). Remnants of Moldanubian HP-HT granulites in the eastern part of the Bavarian Forest (southwestern Bohemian Massif): Evidence from SHRIMP zircon dating and whole rock geochemistry. *Zeitschrift der Deutschen Gesellschaft für Geowissenschaften*, *163*(2), 137–152. https://doi.org/10.1127/1860-1804/2012/0163-0137

Tessin, R. (1989). *Geologische Karte von Mittelsachsen ohne Känozoikum*. Berlin, Germany: Zentrales Geologisches Institut.

Tichomirowa, M., & Köhler, R. (2013). Discrimination of protolithic versus metamorphic zircon ages in eclogites: Constraints from the Erzgebirge metamorphic core complex (Germany). *Lithos*, *177*, 436–450. https://doi.org/10.1016/j.lithos.2013.07.013

Tichomirowa, M., Sergeev, S., Berger, H.-J., & Leonhardt, D. (2012). Inferring protoliths of high-grade metamorphic gneisses of the Erzgebirge using zirconology, geochemistry and comparison with lower-grade rocks from Lusatia (Saxothuringia, Germany). *Contributions to Mineralogy and Petrology*, *164*, 375–396. https://doi.org/10.1007/s00410-012-0742-8

Timmermann, H., Štědrá, V., Gerdes, A., Noble, S. R., Parrish, R. R., & Dörr, W. (2004). The problem of dating high-pressure metamorphism: A U-Pb isotope and geochemical study on eclogites and related rocks of the Mariánské Lázně Complex, Czech Republic. *Journal of Petrology*, *45*, 1311–1338.

Trail, D., Watson, E. B., & Tailby, N. D. (2012). Ce and Eu anomalies in zircon as proxies for the oxidation state of magmas. *Geochimica et Cosmochimica Acta*, *97*, 70–87. https://doi.org/10.1016/j.gca.2012.08.032

Vavra, G., & Reinhardt, J. (1997). Which processes are dated by U/Pb zircon ages of high-grade metamorphic rocks? Zircon genesis in various lithologies and structural levels of the Saxonian Granulite Massif. *Terra Nostra*, *5*(97), 190–192.

Vavra, G., Reinhardt, J., & Pidgeon, R. T. (1999). Lower Carboniferous (340 Ma) HP/HT-metamorphism and rapid exhumation of the Saxonian Granulite Massif. *Terra Nostra*, *1*(99), 203.

Vielzeuf, D., & Schmidt, M. W. (2001). Melting relations in hydrous systems revisited: Application to metapelites, metagreywackes and metabasalts. *Contributions to Mineralogy and Petrology*, *141*, 251–267. https://doi.org/10.1007/s004100100237

Villa, I. M. (1998). Isotopic closure. *Terra Nova*, *10*, 42–47. https://doi.org/10.1046/j.1365-3121.1998.00156.x

von Quadt, A. (1993). The saxonian granulite massif: New aspects from geochronological studies. *International Journal of Earth Sciences*, *82*, 516–530. https://doi.org/10.1007/BF00212414

von Quadt, A., & Günther, D. (1999). Evolution of Cambrian eclogitic rocks in the Erzgebirge: A conventional and LA-ICP-MS U-Pb zircon and Sm-Nd study. *Terra Nostra*, *99*(1), 164.

Walter, H. (2006). Das Rotliegend der Nordwestsächsischen Senke. *Veröffentlichungen des Museums für Naturkunde Chemnitz*, *29*, 157–176.

Watson, E. B., & Harrison, T. M. (1983). Zircon saturation revisited: Temperature and composition effects in a variety of crustal magma types. *Earth and Planetary Science Letters*, *64*, 295–304. https://doi.org/10.1016/0012-821X(83)90211-X

Werner, O. (1998). K-Ar- und Rb-Sr-Chronologie spätvariscischer Krustenkonvergenz – Bilanzierung des Wärme- und Stofftransportes im Erzgebirge. Doctoral thesis Universität Heidelberg, Heidelberg. 199 pp.

Werner, O., & Reich, S. (1997). $^{40}Ar/^{39}Ar$-Abkühlalter von Gesteinen mit unterschiedlicher P-T-Entwicklung aus dem Schiefermantel des Sächsischen Granulitgebirges. *Terra Nostra*, *5*(97), 196–198.

Whitney, D. L., & Evans, B. W. (2010). Abbreviations for names of rock-forming minerals. *American Mineralogist*, *95*, 185–187. https://doi.org/10.2138/am.2010.3371

Winchester, J. A., Floyd, P. A., Chocyk, M., Horbowy, K., & Kozdroj, W. (1995). Geochemistry and tectonic environment of Ordovician meta-igneous rocks in the Rudawy Janowickie Complex, SW Poland. *Journal of the Geological Society, London*, *152*, 105–115. https://doi.org/10.1144/gsjgs.152.1.0105

Wirth, C. (1989). Vergleichende geochemische und mineralogische Untersuchungen an Gabbros und Diabasen des Sächsischen Granulitgebirges. Doctoral thesis. Technische Universität Bergakademie Freiberg, Freiberg. 101 pp.

Zack, T., Moraes, R., & Kronz, A. (2004). Temperature dependence of Zr in rutile: Empirical calibration of a rutile thermometer. *Contributions to Mineralogy and Petrology*, *148*, 471–488. https://doi.org/10.1007/s00410-004-0617-8

SUPPORTING INFORMATION

Additional supporting information may be found online in the Supporting Information section.

Appendix S1: Analytical methods

Appendix S2: Sample locality list

Appendix S3: Amphibole composition data

Appendix S4: Biotite composition data
Appendix S5: White mica composition data
Appendix S6: Garnet composition data
Appendix S7: Plagioclase composition data
Appendix S8: Zircon U–Th–Pb isotopic data
Appendix S9: Zircon rare earth element data
Appendix S10: Ti-in-zircon thermometry data
Appendix S11: $^{40}Ar/^{39}Ar$ amphibole step-heating data
Appendix S12: $^{40}Ar/^{39}Ar$ mica step-heating data
Figure S1: Hand specimen photos of rocks of the SGM
Figure S2: Microtextures of felsic granulites of the SGM
Figure S3: Microtextures of mafic granulites of the SGM
Figure S4: Microtextures of metapelites of the SGM

How to cite this article: Rötzler J, Timmerman MJ. Geochronological and petrological constraints from the evolution in the Saxon Granulite Massif, Germany, on the Variscan continental collision orogeny. *J Metamorph Geol*. 2020;00:1–36. https://doi.org/10.1111/jmg.12559